Combined heat and mass transfer and thermodynamic irreversibilities in the stagnation-point flow of Casson rheological fluid over a cylinder with catalytic reactions and inside a porous medium under local thermal nonequilibrium

Rasool Alizadeh [1], Sina Rezaei Gomari[2,*], Ahmad Alizadeh[3], Nader Karimi[4], Larry K.B. Li[5]

[1] Department of Mechanical Engineering, Quchan Branch, Islamic Azad University, Quchan, Iran

[2] School of Science, Engineering and Design, Teesside University, TS13BA, United Kingdom

[3] Young Researchers Club, Quchan Branch, Islamic Azad University, Quchan, Iran

[4]School of Engineering, University of Glasgow, Glasgow G12 8QQ, United Kingdom

[5]Department of Mechanical and Aerospace Engineering, The Hong Kong University of Science and Technology, Clear Water Bay, Hong Kong, Email: larryli@ust.hk

Abstract

The transport of heat and mass from the surface of a cylinder coated with a catalyst and subject to an impinging flow of a Casson rheological fluid is investigated. The cylinder features circumferentially non-uniform transpiration and is embedded inside a homogenous porous medium. The non-equilibrium thermodynamics of the problem, including Soret and Dufour effects and local thermal non-equilibrium in the porous medium, are considered. Through the introduction of similarity variables, the governing equations are reduced to a set of non-linear ordinary differential equations which are subsequently solved numerically. This results in the prediction of hydrodynamic, temperature, concentration and entropy generation fields, as well as local and average Nusselt, Sherwood and Bejan numbers. It is shown that, for low values of the Casson parameter and thus strong non-Newtonian behaviour, the porous system has a significant tendency towards maintaining local thermal equilibrium. Furthermore, the results show a major reduction in the average Nusselt number during the transition from Newtonian to non-Newtonian fluid, while the reduction in the Sherwood number is less pronounced. It is also demonstrated that flow, thermal and mass transfer irreversibilities are significantly affected by the fluid's strengthened non-Newtonian characteristics. The physical reasons for these behaviours are discussed by exploring the influence of the Casson parameter and other pertinent factors upon the thickness of thermal and concentration boundary layers. It is noted that this study is the first systematic investigation of the stagnation-point flow of Casson fluid in cylindrical porous media.

Keywords: Casson fluid, Stagnation-point flow; Local thermal non-equilibrium, Entropy generation, Similarity solution, Soret effect, Dufour effect.

* Corresponding Author: Sina Rezaei Gomari, s.rezaei-gomari@tees.ac.uk

Nomenclature

a	cylinder radius	$\dddot{S}_D$	rate of entropy generation due to mass transfer
a_{sf}	interfacial area per unit volume of porous media	$\dddot{S}_0$	characteristic entropy generation rate
Be	Bejan number	$\dddot{S}_{gen}$	rate of entropy generation
Bi	Biot number $Bi = \frac{h_{sf} a_{sf}.a}{4k_f}$	Sr	Soret number $Sr = \frac{D.k_T}{T_\infty}\frac{(T_W - T_\infty)}{C_\infty.\alpha}$
Br	Brinkman number $Br = \frac{\mu_f(\bar{k}.a)^2}{k_f(T_W - T_\infty)}$	Sh	Sherwood number
C	fluid concentration	T	temperature
C_p	specific heat at constant pressure	T_m	mean fluid temperature
C_s	concentration susceptibility	$u\,, w$	velocity components along $(r - \varphi - z)$-axis
D	molecular diffusion coefficient	$U_0(\varphi)$	transpiration
Df	Dufour number $Df = \frac{D.k_T}{C_s.C_p}\frac{C_\infty}{(T_W - T_\infty)\upsilon}$	z	axial coordinate
$f(\eta, \varphi)$	function related to u-component of velocity	**Greek symbols**	
h	heat transfer coefficient	α	thermal diffusivity
h_{sf}	fluid-to-solid heat transfer coefficient	β	Casson fluid parameter
k	thermal conductivity	γ	modified conductivity ratio $\gamma = \frac{k_f}{k_s}$
$\bar{k}$	freestream strain rate	γ^*	Damköhler number $\gamma^* = \frac{k_R.a}{2D}\frac{1}{C_\infty}$
k_m	mass transfer coefficient	δ	constant parameter $\delta = \frac{R_g.D.C_\infty}{k_f}$
k_R	Kinetic constant	ε	porosity
k_T	thermal diffusion ratio	η	similarity variable, $\eta = \left(\frac{r}{a}\right)^2$
k_1	permeability of the porous medium	$\theta(\eta, \varphi)$	non-dimensional temperature
N_{GT}	entropy generation number due to heat transfer $N_{GT} = \frac{\dddot{S}_T}{\dddot{S}_0}$	Λ	dimensionless temperature difference $\Lambda = \frac{(T_W - T_\infty)}{T_\infty}$
N_{GF}	entropy generation number due to fluid friction $N_{GF} = \frac{\dddot{S}_f}{\dddot{S}_0}$	λ	Permeability parameter, $\lambda = \frac{a^2}{4k_1}$
N_{GD}	entropy generation number due to mass transfer $N_{GD} = \frac{\dddot{S}_D}{\dddot{S}_0}$	μ	dynamic viscosity
Nu	Nusselt number	μ_B	plastic dynamic viscosity of the considered fluid
p	fluid pressure	υ	kinematic viscosity

P	non-dimensional fluid pressure	π	component of deformation rate
P_0	initial fluid pressure	π_c	critical value of deformation rate
Pr	Prandtl number	ρ	fluid density
p_y	yield stress of the fluid	τ	component of the stress tensor
q_m	mass flow at the wall	σ	shear stress
q_w	heat flow at the wall	ϕ	non-dimensional fluid concentration
r	radial coordinate	φ	angular coordinate
Re	Freestream Reynolds number $Re = \frac{\bar{k}.a^2}{2\upsilon}$		
R_g	gas constant	**Subscripts**	
$S(\varphi)$	transpiration rate function $S(\varphi) = \frac{U_0(\varphi)}{\bar{k}.a}$	w	condition on the surface of the cylinder
Sc	Schmidt number $Sc = \frac{\upsilon}{D}$	∞	far field
$\dddot{S}_f$	rate of entropy generation due to fluid friction	f	fluid
$\dddot{S}_T$	rate of entropy generation due to heat transfer	s	solid

1. Introduction

The flow of non-Newtonian fluid through porous media has recently been highlighted as an area with a substantial need for further exploration [1]. This is primarily due to the wide and increasing applications of non-Newtonian fluids in a number of technological fields [2]. It also stems from scientific curiosity due to the rich behaviour of non-Newtonian fluids, which are still not fully understood [3]. Stagnation-point flows in porous media are also of high importance, particularly in the context of heat and mass transfer. This problem has already been investigated extensively, while major emphasis has been placed on the heat transfer process, see e.g. [4, 5, 6]. However, the specific problems of the impinging external flow of a non-Newtonian fluid upon stretching surfaces and porous inserts are relatively new and still significantly unexplored. A survey of literature in this area is presented below in which, for reasons of brevity, only studies specifically of Casson fluid are discussed.

The problem of the stagnation-point flow and heat transfer of Casson fluid over a stretching sheet was investigated by Mustafa et al. [7]. Their study was concerned with the heat transfer characteristics of such a configuration. These authors used similarity parameters to reduce the governing equations to coupled ordinary differential equations, and subsequently applied homotopy analysis[7]. Hayat et al [8] studied the Soret and Dufour effects on magnetohydrodynamic flow of Casson fluid on a stretching plate. It was demonstrated that decreases in the Casson parameter led to reductions in temperature and concentration. Malik et al. [9]. carried out a study on the boundary layer flow of a Casson nanofluid over a radially stretching cylinder. Nadeem et al. [10] presented the boundary layer flow of a Casson nanofluid flow over a stretching plate. Magnetohydrodynamic effects were included and three-dimensional equations were solved numerically. Comparing the Newtonian and non-Newtonian fluids, an increase of about 5% was reported in the value of the Nusselt number in the case of Casson fluid [10]. Entropy generation in the flow of Casson fluid in a boundary layer was first modelled by Abolbashari et al. [11]. Abolbashari et al. showed that increasing the Casson fluid parameter led to a reduction in fluid velocity. Furthermore, it caused a slight enhancement in the thickness of the thermal and concentration boundary layers [11]. Moreover, decreasing the Casson parameter, and thus strengthening the non-Newtonian characteristics of

the fluid, intensified the generation of entropy within the system. The unsteady natural convection of Casson fluid passing through a vertical porous insert subject to constant wall temperature was investigated by Khalid et al. [12], who showed that the Nusselt number decreased as time elapsed.

Abbas et al. discussed the combined heat and mass transfer in an unsteady, chemically reactive boundary layer flow over a stretching surface [13]. A linear model of thermal radiation together with temperature- dependent Arrhenius chemical kinetics were added to the unsteady, two-dimensional equations of mass, momentum, energy and chemical species transport. It was observed that increases in the Casson fluid parameter (approaching Newtonian fluid) led to decreases in the thickness of the momentum, thermal and concentration boundary layers [13]. It was also shown that the thickness of the concentration boundary layer decreased with the augmentation of the chemical reaction rate and increasing the temperature difference between the wall and free fluid[13]. In a theoretical investigation, Hakeem et al. analysed the boundary layer flow of Casson fluid in the presence of magnetic effects and thermal radiation [14]. The authors argued that skin friction increases with the Casson and velocity slip parameters and that these parameters reduce the Nusselt number and increase wall temperature. Rauf et al. [15] investigated the three-dimensional double-diffusive convection of the chemically reactive boundary layer flow of Casson fluid with magnetic effects over a stretching surface. This study revealed that enhancements of the Casson parameter increased the shear stress induced on the surface [15].

In recent work, Khan et al. [16] considered the boundary layer flow of a Casson fluid over a stretching surface with a catalytic chemical reaction on the surface together with a homogenous autocatalytic reaction within the fluid. The heat of reaction and magnetohydrodynamic effects were also added to this analysis. Using a similarity solution procedure, it was shown that the surface drag force increased with larger magnetic intensity, while the heat transfer rate decayed at higher values of the Prandtl number [16]. In an attempt to develop a model for the motion of dusty fluids, Ramesh et al. [17] investigated the forced convection of Casson fluid on the surface a stretching cylinder. The authors also added the effects of a secondary particle phase, an imposed magnetic field and thermal radiation. It was demonstrated that an increase in the Casson parameter led to the reduction of the temperature in the two phases investigated. Mixed convection in an oblique stagnation flow of Casson fluid was recently investigated by Rana et al. [18]. This work included partial slip as well as heterogenous and homogenous chemical reactions which provide internal heating. Amongst other findings, Rana et al. showed that increases in the slip parameter reduced the concentration of chemical species on the surface [18]. Most recently, the magnetohydrodynamics of Casson fluid flow over a rotating disk with the inclusion of chemical reactions, exothermicity and thermal diffusion of chemical species have been analysed by Rehman et al [19].

A few prominent points follow from the above review of the literature. Firstly, a vast majority of existing studies of the stagnation flow of Casson fluid are concerned with flat surfaces in the form of stretching surfaces or rotating disks. Investigations of Casson fluid flows over curved surfaces are much scarcer. Secondly, with the exception of the study of Khalid et al. [12], there is no work on stagnation-point flow over surfaces covered with porous media. Furthermore, the limited number of studies on Casson fluid flow in porous media have considered local thermal equilibrium and hence the influence of non-Newtonian behaviour upon the local thermodynamic equilibrium has been totally ignored. Thirdly, the effects of surface transpiration have hardly been studied at all in the context of the stagnation-point flow of Casson fluid. Finally, the generation of entropy in these flow configurations, and in particular the influence of non-Newtonian behaviour on the irreversibilities encountered, are still almost completely unexplored. To address these shortcomings, the current study considers a stagnation-

point flow of Casson fluid over a cylinder covered by a catalytic coating, featuring circumferentially non-uniform transpiration and embedded in a porous medium. Analyses of combined heat and mass transfer as well as entropy generation are conducted. An attempt is then made to explain the pertinent physical processes.

2. Theoretical and numerical methods

2.1. Problem configuration, assumptions and governing equations

Figure 1 shows a schematic view of the problem under investigation. This includes a cylinder with radius *a* centred at r=0 covered by a porous medium. The external surface of the cylinder may include uniform or non-uniform fluid transpiration in the form of blowing and suction, with prescribed circumferential distributions, and with the temperature of the external surface of the cylinder kept constant. An external axisymmetric radial stagnation-point flow of a non-Newtonian fluid (Casson fluid) with strain rate of $\bar{k}$ impinges on the cylinder. Due to the non-uniformity of transpiration, the flow configuration around the cylinder could be non-axisymmetric. The assumptions made throughout this work are as follows:

- The flow is steady, incompressible and laminar and the cylinder is assumed to be infinitely long.
- A zeroth order, temperature-independent, heterogenous chemical reaction [20, 21] takes place on the external surface of the cylinder.
- The thermal diffusion of chemical species (Soret effect) and transport of energy through mass diffusion (Dufour effect) are considered [22, 23].
- The porous medium is homogenous, isotropic and at local thermal non-equilibrium.
- The radiation heat transfer and viscous dissipation of kinetic energy of the flow are ignored.
- Physical properties such as porosity, specific heat, density and thermal conductivity are assumed to be constant and hence thermal dispersion effects are negligible.
- A moderate range of the pore-scale Reynolds number is considered in the porous medium, and hence non-linear effects in momentum transfer are negligibly small.

The rheological equation for an isotopical, incompressible flow of a Casson fluid is [24]:

$$\tau_{ij} = \begin{cases} 2\left(\mu_B + \dfrac{p_y}{\sqrt{2\pi}}\right)e_{ij} & \pi > \pi_c \\ 2\left(\mu_B + \dfrac{p_y}{\sqrt{2\pi c}}\right)e_{ij} & \pi < \pi_c \end{cases} \tag{1}$$

Here, τ_{ij} is the (i, j)-th component of the stress tensor, $\pi_{ij} = e_{ij}e_{ij}$and e_{ij} are the (i, j)-th component of the deformation rate, π is the product of the component of deformation rate with itself, π_c is a critical value of this product based on the non-Newtonian model, μ_B is the plastic dynamic viscosity of the considered fluid and p_y is the yield stress of the fluid. Therefore, if the applied shear stress is less than the yield stress, the non-Newtonian fluid behaves like a solid, whereas if it is greater then it starts to move. A two-dimensional Darcy-Brinkman model of transport of momentum [5, 25-31] together with the two-equation model of the transport of thermal energy in porous media [32, 33] are used in this work. The governing equations and boundary conditions, in the cylindrical coordinate system shown in Fig. 1, can be summarised as follows.

The continuity of mass reads,

$$\frac{\partial(ru)}{\partial r} + r\frac{\partial w}{\partial z} = 0 \tag{2}$$

The transport of momentum in the radial direction is given the Darcy-Brinkman model:

$$\frac{\rho}{\varepsilon^2}\left(u\frac{\partial u}{\partial r}+w\frac{\partial u}{\partial z}\right)=-\frac{\partial p}{\partial r}+\frac{\mu}{\varepsilon}\left(1+\frac{1}{\beta}\right)\left(\frac{\partial^2 u}{\partial r^2}+\frac{1}{r}\frac{\partial u}{\partial r}-\frac{u}{r^2}+\frac{1}{r^2}\frac{\partial^2 u}{\partial \varphi^2}+\frac{\partial^2 u}{\partial z^2}\right)-\frac{\mu}{k_1}\left(1+\frac{1}{\beta}\right)u. \tag{3}$$

Similarly, the transport of momentum in the axial direction takes the form of:

$$\frac{\rho}{\varepsilon^2}\left(u\frac{\partial w}{\partial r}+w\frac{\partial w}{\partial z}\right)=-\frac{\partial p}{\partial z}+\frac{\mu}{\varepsilon}\left(1+\frac{1}{\beta}\right)\left(\frac{\partial^2 w}{\partial r^2}+\frac{1}{r}\frac{\partial w}{\partial r}+\frac{1}{r^2}\frac{\partial^2 w}{\partial \varphi^2}+\frac{\partial^2 w}{\partial z^2}\right)-\frac{\mu}{k_1}\left(1+\frac{1}{\beta}\right)w \tag{4}$$

The transport of thermal energy in the fluid phase is expressed by [22, 23, 33],

$$u\frac{\partial T_f}{\partial r}+w\frac{\partial T_f}{\partial z}=\alpha_f\left(\frac{\partial^2 T_f}{\partial r^2}+\frac{1}{r}\frac{\partial T_f}{\partial r}+\frac{1}{r^2}\frac{\partial^2 T_f}{\partial \varphi^2}+\frac{\partial^2 T_f}{\partial z^2}\right)+h_{sf}\,.\,a_{sf}\left(T_s-T_f\right)+\frac{D\,k_T}{C_s\,.\,C_p}\left(\frac{\partial^2 C}{\partial r^2}+\frac{1}{r}\frac{\partial C}{\partial r}+\frac{1}{r^2}\frac{\partial^2 C}{\partial \varphi^2}+\frac{\partial^2 C}{\partial z^2}\right), \tag{5}$$

while the transport of thermal energy in the solid phase is written as [32, 33]:

$$k_s\left(\frac{\partial^2 T_s}{\partial r^2}+\frac{1}{r}\frac{\partial T_s}{\partial r}+\frac{1}{r^2}\frac{\partial^2 T_s}{\partial \varphi^2}+\frac{\partial^2 T_s}{\partial z^2}\right)-h_{sf}\,.\,a_{sf}\left(T_s-T_f\right)=0. \tag{6}$$

The transport of the chemical species is governed by the following advective-diffusive model which takes into account contributions from the Soret and Dufour effects in addition to the Fickian diffusion of species [21, 22]:

$$u\frac{\partial C}{\partial r}+w\frac{\partial C}{\partial z}=D\left(\frac{\partial^2 C}{\partial r^2}+\frac{1}{r}\frac{\partial C}{\partial r}+\frac{1}{r^2}\frac{\partial^2 C}{\partial \varphi^2}+\frac{\partial^2 C}{\partial z^2}\right)+\frac{D\,k_T}{T_m}\left(\frac{\partial^2 T_f}{\partial r^2}+\frac{1}{r}\frac{\partial T_f}{\partial r}+\frac{1}{r^2}\frac{\partial^2 T_f}{\partial \varphi^2}+\frac{\partial^2 T_f}{\partial z^2}\right). \tag{7}$$

As also defined in the nomenclature, in Eqs. (2-7) p, ρ, μ, T, α_f, k_T, $\beta=\mu_B\frac{\sqrt{2\pi_C}}{P_y}$, are the pressure, density, kinematic viscosity of the fluid, temperature, thermal diffusivity of the fluid, thermal diffusion ratio, Casson fluid parameter, respectively. Further, ε and k_1 represent porosity and permeability of the porous medium, respectively. The flow characteristics are evaluated inside the boundary layer and in the vicinity of the flow impingement point. In Eq. (5-7) the subscripts "f" and "s", refer to fluid and solid properties, respectively.

The velocity boundary conditions for the momentum Eqs. (3,4) are as follows.

$$r=a:\quad w=0\,,\quad u=-U_0(\varphi), \tag{8}$$

$$r=\infty:\quad w=2\bar{k}z\,,\quad u=-\bar{k}\left(r-\frac{a^2}{r}\right). \tag{9}$$

Further, the two boundary conditions with respect to φ (angular coordinate) are expressed as:

$$u(r,0)=u(r,2\pi)\,,\quad \frac{\partial u(r,0)}{\partial \varphi}=\frac{\partial u(r,2\pi)}{\partial \varphi}. \tag{10}$$

Equation 8 represents the no-slip condition on the external surface of the cylinder. Furthermore, Eq. 9 indicates that the viscous flow solution approaches, in a manner analogous to the Hiemenz flow, the potential flow solution as $r\to\infty$ [26, 27, 30, 31, 34]. This can be verified by starting from the continuity equation in the following, $-\frac{1}{r}\frac{\partial(ru)}{\partial r}=\frac{\partial w}{\partial z}$ Constant $=2\bar{k}z$ and integrating in the r and z directions with boundary conditions, $w=0$ when $z=0$ and $u=-U_0(\varphi)$ when $r=a$.

The boundary conditions for the transport of thermal energy Eqs. (5,6) is given by

$$r=a:\quad T_f=T_w=\text{Constant},$$

$$T_s = T_w = \text{Constant}, \tag{11}$$

$r = \infty$: $T_f = T_\infty$,

$T_s = T_\infty$,

and the two boundary conditions with respect to the angular coordinate, φ are

$$T_f(r,0) = T_f(r,2\pi)\,,\ \ T_s(r,0) = T_s(r,2\pi), \tag{12}$$

$$\frac{\partial T_f(r,0)}{\partial \varphi} = \frac{\partial T_f(r,2\pi)}{\partial \varphi}\,, \quad \frac{\partial T_s(r,0)}{\partial \varphi} = \frac{\partial T_s(r,2\pi)}{\partial \varphi},$$

in which T_w is the cylinder surface temperature and T_∞ is the free-stream temperature.

The boundary conditions for the transport of chemical species Eq. (7) are as follows

$$r = a: \quad \frac{\partial C}{\partial r} = -\frac{k_R}{D} = \text{Constant}, \tag{13}$$

$r = \infty$: $C \to C_\infty$,

in which, D is the molecular diffusion coefficient and k_R is the kinetic constant pertinent to the heterogenous chemical reaction, and the two boundary conditions with respect to the angular coordinate, φ are

$$C(r,0) = C(r,2\pi), \tag{14}$$

$$\frac{\partial C(r,0)}{\partial \varphi} = \frac{\partial C(r,2\pi)}{\partial \varphi},$$

in which C_w is the cylinder surface concentration and C_∞ is the free-stream concentration.

2.2 Self-similar solutions

A reduction of the governing Eqs. (2-7) is obtained by applying the following similarity transformations:

$$u = -\frac{\bar{k}.a}{\sqrt{\eta}} f(\eta,\varphi)\,, \qquad w = \left[2\bar{k}\acute{f}(\eta,\varphi)\right]z\,, \qquad p = \rho_f \bar{k}^2 a^2 P, \tag{15}$$

where $\eta = \left(\frac{r}{a}\right)^2$ the dimensionless radial variable. Transformation 15 satisfies Eq. 2 automatically and their substitution into Eqs. 3 and 4 leads to the following system of coupled differential equations:

$$\varepsilon.\left(1+\frac{1}{\beta}\right)\left[\eta\dddot{f} + \ddot{f} + \frac{1}{4\eta}\frac{\partial^2 \acute{f}}{\partial \varphi^2}\right] + Re\left[1 + f\acute{f} - \left(\acute{f}\right)^2\right] + \varepsilon^2.\lambda.\left(1+\frac{1}{\beta}\right)\left[1-\acute{f}\right] = 0 \tag{16}$$

$$P - P_0 = -\frac{1}{2\varepsilon^2}\left(\frac{f^2}{\eta}\right) - \frac{1}{\varepsilon}\left(1+\frac{1}{\beta}\right)\left[\left(\frac{\acute{f}}{Re} - \frac{1}{4Re}\int_1^\eta \frac{1}{\eta^2}\frac{\partial^2 f}{\partial \varphi^2}d\eta\right) + \frac{\lambda}{Re}\int_1^\eta \frac{f}{\eta}d\eta\right] - 2\left[\frac{1}{\varepsilon^2} + \frac{\lambda}{Re}\left(1+\frac{1}{\beta}\right)\right]\left(\frac{z}{a}\right)^2, \tag{17}$$

in which $Re = \frac{\bar{k}.a^2}{2\upsilon}$ is the freestream Reynolds number, $\lambda = \frac{a^2}{4k_1}$ is referred to as permeability parameter and prime indicates differentiation with respect toη. Considering Eqs. (8), (9), and (10), the boundary conditions for Eqs. (16) and (17) reduce to:

$$\eta = 1: \qquad \acute{f}(1,\varphi) = 0\,, \qquad f(1,\varphi) = S(\varphi), \tag{18}$$

$$\eta \to \infty: \qquad \acute{f}(\infty,\varphi) = 0, \tag{19}$$

$$f(\eta,0)=f(\eta,2\pi)\ ,\ \frac{\partial f(\eta,0)}{\partial\varphi}=\frac{\partial f(\eta,2\pi)}{\partial\varphi},\tag{20}$$

in which, $S(\varphi)=\frac{U_0(\varphi)}{k.a}$ is the transpiration rate function. It is noted that Eqs. 16 and 17 are the complete forms of Eqs. 9 and 11 in the study by Saleh & Rahimi [35]. To reduce the energy Eq. (4) to a dimensionless form, the following transformation is introduced,

$$\theta_f(\eta,\varphi)=\frac{T_f(\eta,\varphi)-T_\infty}{T_w-T_\infty}.\tag{21}$$

The substitution of Eqs. 15 and 21 into Eq. 5 and ignoring the small dissipation terms yields:

$$\eta\acute{\theta}_f+\acute{\theta}_f+\frac{1}{4\eta}\frac{\partial^2\theta_f}{\partial\varphi^2}+Re.Pr.\left(f.\acute{\theta}_f\right)+Bi\left(\theta_s-\theta_f\right)+Df.Pr\left[\eta\acute{\phi}+\acute{\phi}+\frac{1}{4\eta}\frac{\partial^2\phi}{\partial\varphi^2}\right]=0,\tag{22}$$

in which, $Bi=\frac{h_{sf}a_{sf}.a^2}{4k_f}$ and $Df=\frac{D.k_T}{C_s.C_p}\frac{C_\infty}{(T_w-T_\infty)\upsilon}$ are the Biot and Dufour numbers, respectively. Further, the boundary conditions reduce to:

$$\eta=1:\qquad\theta_f(1,\varphi)=1,\tag{23a}$$

$$\eta\to\infty:\qquad\theta_f(\infty,\varphi)=0,\tag{23b}$$

$$\theta_f(\eta,0)=\theta_f(\eta,2\pi)\ ,\ \frac{\partial\theta_f(\eta,0)}{\partial\varphi}=\frac{\partial\theta_f(\eta,2\pi)}{\partial\varphi}.\tag{24a,b}$$

Substitution of Eqs. (15) and (21) into Eq. (6) yields

$$\eta\acute{\theta}_s+\acute{\theta}_s+\frac{1}{4\eta}\frac{\partial^2\theta_s}{\partial\varphi^2}-Bi.\gamma\left(\theta_s-\theta_f\right)=0,\tag{25}$$

in which, $\gamma=\frac{k_f}{k_s}$ is the modified conductivity ratio, and the boundary conditions reduce to:

$$\eta=1:\qquad\theta_s(1,\varphi)=1,\tag{26a}$$

$$\eta\to\infty:\qquad\theta_s(\infty,\varphi)=0,\tag{26b}$$

$$\theta_s(\eta,0)=\theta_s(\eta,2\pi)\ ,\ \frac{\partial\theta_s(\eta,0)}{\partial\varphi}=\frac{\partial\theta_s(\eta,2\pi)}{\partial\varphi}.\tag{27a,b}$$

To transform the mass transfer Eq. (7) into a dimensionless form, the following transformation is introduced:

$$\phi(\eta,\varphi)=\frac{C(\eta,\varphi)-C_\infty}{C_\infty}.\tag{28}$$

After the substitution of Eqs. 15 and 21 into Eq. 7 and some algebraic manipulation, the following differential equation results:.

$$Pr\left[\eta\acute{\phi}+\acute{\phi}+\frac{1}{4\eta}\frac{\partial^2\phi}{\partial\varphi^2}\right]+Sr.Sc\left[\eta\acute{\theta}_f+\acute{\theta}_f+\frac{1}{4\eta}\frac{\partial^2\theta_f}{\partial\varphi^2}\right]+Re.Pr.Sc\left(f.\acute{\phi}\right)=0,\tag{29}$$

in which, $Sc=\frac{\upsilon}{D}$ is the Schmidt number and $Sr=\frac{D.k_T}{T_m}\frac{(T_w-T_\infty)}{C_\infty.\alpha}$ is the Soret number, while the boundary conditions reduce to:

$$\eta=1:\qquad\acute{\phi}(1,\varphi)=-\gamma^*,\tag{30a}$$

$$\eta\to\infty:\qquad\phi(\infty,\varphi)=0,\tag{30b}$$

in which, $\gamma^*=\frac{k_R.a}{2D}\frac{1}{C_\infty}$ is the Damköhler number

$$\phi(\eta,0)=\phi(\eta,2\pi)\ ,\ \ \frac{\partial\phi(\eta,0)}{\partial\varphi}=\frac{\partial\phi(\eta,2\pi)}{\partial\varphi}. \tag{31a,b}$$

It is recalled here that Eq. 22 is the complete form of Saleh & Rahimi's Equation 14 [35]. Eqs. 16, 22, 25 and 29, together with the boundary conditions in Eqs. 18-20, 23-24, 26-27, 30 and 31, are solved numerically using an implicit, iterative tri-diagonal finite-difference method similar to that discussed in previous work [36, 37] .

2.3 Shear stress, Nusselt number and Sherwood number

The shear-stress induced by the nanofluid flow on the external surface of the cylinder is given by:

$$\sigma=\mu\left(1+\frac{1}{\beta}\right)\left[\frac{\partial w}{\partial r}\right]_{r=a}, \tag{32}$$

where μ is the viscosity. Employing Eq. (15), a semi-similar solution for the shear stress on the surface of the cylinder can be developed. This reads:

$$\sigma=\mu\left(1+\frac{1}{\beta}\right)\frac{2}{a}\left[2\bar{k}z\acute{f}(1,\varphi)\right]\Rightarrow\frac{\sigma.a}{4\mu\bar{k}z}=\left(1+\frac{1}{\beta}\right)\acute{f}(1,\varphi). \tag{33}$$

For the current problem with iso-thermal boundaries, the local heat convection coefficient and rate of heat transfer for the fluid phase are defined as:

$$h=\frac{q_w}{T_w-T_\infty}=\frac{-k_f\left(\frac{\partial T_f}{\partial r}\right)_{r=a}}{T_w-T_\infty}=-\frac{2k_f}{a}\frac{\partial\theta_f(1,\varphi)}{\partial\eta}, \tag{34}$$

and

$$q_w=-\frac{2k_f}{a}\frac{\partial\theta_f(1,\varphi)}{\partial\eta}T_w-T_\infty. \tag{35}$$

Hence, Nusselt number for fluid phase can be written as:

$$Nu=\frac{h.a}{2k_f}=-\acute{\theta}(1,\varphi). \tag{36}$$

Similarly, the local mass transfer coefficient and rate of mass transfer are defined as:

$$k_m=\frac{q_m}{C_w-C_\infty}=\frac{-D\left(\frac{\partial C}{\partial r}\right)_{r=a}}{C_w-C_\infty}=-\frac{2D}{a}\frac{\partial\phi(1,\varphi)}{\partial\eta}, \tag{37}$$

and

$$q_m=-\frac{2D}{a}\frac{\partial\phi(1,\varphi)}{\partial\eta}C_w-C_\infty. \tag{38}$$

Hence, Sherwood number is given by:

$$Sh=\frac{k_m.a}{2D}=-\acute{\phi}(1,\varphi). \tag{39}$$

2.4- Entropy generation

Considering the assumptions stated in section 2.1, the volumetric rate of local entropy generation in the problem is given by [38, 39, 40]:

$$\dddot{S}_{gen}=\dddot{S}_f+\dddot{S}_T+\dddot{S}_D,$$

$$\dddot{S}_f = \frac{2\mu}{T_\infty}\left(1+\frac{1}{\beta}\right)\left[\left(\frac{\partial u}{\partial r}\right)^2+\left(\frac{u}{r}\right)^2+\left(\frac{\partial w}{\partial z}\right)^2\right]+\frac{\mu}{T_\infty}\left(1+\frac{1}{\beta}\right)\left[\left(\frac{1}{r}\frac{\partial w}{\partial \varphi}\right)^2+\left(\frac{\partial w}{\partial r}\right)^2+\left(\frac{1}{r}\frac{\partial u}{\partial \varphi}\right)^2\right]$$
$$+\frac{\mu}{k_1 T_\infty}\left(1+\frac{1}{\beta}\right)[u^2+w^2],$$
$$\dddot{S}_T = \frac{k_f}{{T_f}^2}\left[\left(\frac{\partial T_f}{\partial r}\right)^2+\left(\frac{1}{r}\frac{\partial T_f}{\partial \varphi}\right)^2\right]+\frac{k_s}{{T_s}^2}\left[\left(\frac{\partial T_s}{\partial r}\right)^2+\left(\frac{1}{r}\frac{\partial T_s}{\partial \varphi}\right)^2\right]+h_{sf}a_{sf}(T_s-T_f)\left[\frac{1}{T_f}-\frac{1}{T_s}\right], \quad (40)$$
$$\dddot{S}_D = \frac{R_g.D}{C}\left[\left(\frac{\partial C}{\partial r}\right)^2+\left(\frac{1}{r}\frac{\partial C}{\partial \varphi}\right)^2\right]+\frac{R_g.D}{T_f}\left[\frac{\partial C}{\partial r}\frac{\partial T_f}{\partial r}-\frac{1}{r^2}\frac{\partial C}{\partial \varphi}\frac{\partial T_f}{\partial \varphi}\right].$$

Using the similarly variables given in Eqs. (15) and (40), the local entropy generation becomes:

$$\dddot{S}_T = \frac{4k_f.(T_w-T_\infty)^2}{a^2.T_f^2}\left[\eta\acute{\theta}_f{}^2+\frac{1}{4\eta^2}\left(\frac{\partial \theta_f}{\partial \varphi}\right)^2\right]+\frac{4k_s.(T_w-T_\infty)^2}{a^2.T_s^2}\left[\eta\acute{\theta}_s{}^2+\frac{1}{4\eta^2}\left(\frac{\partial \theta_s}{\partial \varphi}\right)^2\right]$$
$$+\frac{\bar{k}.a^3.a_{sf}.h_{sf}.T_\infty}{8k_f.(T_w-T_\infty)\upsilon}(\theta_f-\theta_s)\left[\frac{1}{\Lambda\theta_f+1}-\frac{1}{\Lambda\theta_s+1}\right],$$
$$\dddot{S}_f = \frac{4\bar{k}^2.\mu}{T_\infty}\left(1+\frac{1}{\beta}\right)\left\{\left[\eta\acute{f}^2+4\acute{f}^2+\left(\frac{f}{\eta}\right)^2-2\frac{f\acute{f}}{\eta}+\frac{1}{\eta}\left(\frac{\partial \acute{f}}{\partial \varphi}\right)^2+\frac{1}{4\eta^2}\left(\frac{\partial f}{\partial \varphi}\right)^2\right]\right. \quad (41)$$
$$\left.+\frac{a^2}{4k_1}\left[\left(\frac{f}{\eta}\right)^2+4\acute{f}^2\right]\right\},$$
$$\dddot{S}_D = \frac{R_g.D.C_\infty}{k_f}\frac{\bar{k}.a^2.T_\infty^2}{2(T_w-T_\infty)^2\upsilon}\frac{1}{(\phi+1)}\left[\eta\acute{\phi}^2+\frac{1}{4\eta^2}\left(\frac{\partial \phi}{\partial \varphi}\right)^2\right]$$
$$+\frac{R_g.D.C_\infty}{k_f}\frac{\bar{k}.a^2.T_\infty}{2(T_w-T_\infty)\upsilon}\frac{1}{\left(\frac{T_w-T_\infty}{T_\infty}\theta_f+1\right)}\left[\eta.\acute{\phi}.\acute{\theta}_f-\frac{1}{4\eta^2}\left(\frac{\partial \phi}{\partial \varphi}\right)\left(\frac{\partial \theta_f}{\partial \varphi}\right)\right],$$

in which $N_{GT}=\frac{\dddot{S}_T}{\dddot{S}_0}$, $N_{GF}=\frac{\dddot{S}_f}{\dddot{S}_0}$, $N_{GD}=\frac{\dddot{S}_D}{\dddot{S}_0}$ and $\dddot{S}_0=\frac{8k_f.(T_w-T_\infty)^2\upsilon}{\bar{k}.a^4.T_\infty^2}$ is the non-dimensional entropy generation respectively by heat transfer, fluid friction, and mass transfer and the characteristic entropy generation rate. The dimensionless form of the volumetric rate of local entropy generation (N_{GT}, N_{GF}, N_{GD}) reduces to the following equations:

$$N_{GT} = \frac{Re}{(\Lambda\theta_f+1)^2}\left[\eta\acute{\theta}_f{}^2+\frac{1}{4\eta^2}\left(\frac{\partial \theta_f}{\partial \varphi}\right)^2\right]+\frac{Re}{\gamma.(\Lambda\theta_s+1)^2}\left[\eta\acute{\theta}_s{}^2+\frac{1}{4\eta^2}\left(\frac{\partial \theta_s}{\partial \varphi}\right)^2\right]$$
$$+\frac{Bi.Re}{\Lambda}(\theta_f-\theta_s)\left[\frac{1}{\Lambda\theta_f+1}-\frac{1}{\Lambda\theta_s+1}\right],$$
$$N_{GF} = \frac{Re.Br}{\Lambda}\left(1+\frac{1}{\beta}\right)\left\{\left[\eta\acute{f}^2+4\acute{f}^2+\left(\frac{f}{\eta}\right)^2-2\frac{f\acute{f}}{\eta}+\frac{1}{\eta}\left(\frac{\partial \acute{f}}{\partial \varphi}\right)^2+\frac{1}{4\eta^2}\left(\frac{\partial f}{\partial \varphi}\right)^2\right]+\lambda\left[\left(\frac{f}{\eta}\right)^2+4\acute{f}^2\right]\right\},$$
$$N_{GD} = \frac{Re.\delta}{\Lambda^2.(\phi+1)}\left[\eta\acute{\phi}^2+\frac{1}{4\eta^2}\left(\frac{\partial \phi}{\partial \varphi}\right)^2\right]+\frac{Re.\delta}{\Lambda.(\Lambda\theta_f+1)}\left[\eta.\acute{\phi}.\acute{\theta}_f-\frac{1}{4\eta^2}\left(\frac{\partial \phi}{\partial \varphi}\right)\left(\frac{\partial \theta_f}{\partial \varphi}\right)\right], \quad (42)$$

where $\Lambda=\frac{(T_w-T_\infty)}{T_\infty}$ is the dimensionless temperature difference, $\delta=\frac{R_g.D.C_\infty}{k_f}$ is the diffusive constant parameter and $Br=\frac{\mu(\bar{k}.a)^2}{k_f(T_w-T_\infty)}$ is the Brinkman number. The Bejan number, defined as the ratio of entropy generation due

to heat and mass transfer to the total entropy generation, is used to facilitate the understanding of the mechanisms of entropy generation. The Bejan number for the current problem can be expressed as:

$$Be = \frac{N_{GT} + N_{GD}}{N_{GF} + N_{GT} + N_{GD}}. \tag{43}$$

2.5 Grid independency and validation

To verify the grid independency of the numerical solution, Table 1 shows the values of the average Nusselt, Sherwood and Bejan numbers for different densities of the computational grid. The mesh densities of 51×18, 102×36, 204×72, 408×144 and 816×288 were investigated. It is clear from Table 1 that there are no considerable changes of Nu_m, Sh_m and Be_m for mesh sizes of (204×72), (408×144) and (816×288). Hence, a (408×144) grid in $\eta - \varphi$ directions was used for the computational domain reported in this work. A non-uniform grid was applied in η-direction to capture the sharp gradients around the external surface of the cylinder, while a uniform mesh was implemented in φ direction. The computational domain extends over $\varphi_{max} = 360°$ and $\eta_{max} = 15$. In this expression, η_{max}corresponds to $\eta \to \infty$, which for all investigated cases, is located outside the momentum boundary layers. Figure 2 shows the computational grid utilised in the current study. A convergence criterion was implemented in the numerical simulations. This was such that when the difference between the two consecutive iterations became less than 10^{-7}, the solution was assumed to have converged and thus computation was terminated. It is also noted that in the current simulations, the numerical error is of $O(\Delta\eta)^2$ [36].

The developed numerical solutions were validated by calculating the radial variations of $\acute{f}$ for different values of β. Figure 3 shows that for large values of β the results of the current simulation approaches closely those of Ref. [5], which corresponds to a similar configuration as Fig. 1 without the catalytic surface and for a Newtonian fluid. Further, in the limit of large β, the average values of dimensionless shear (Table 2) stress are compared favourably with those reported in Ref. [5]. Furthermore, it is expected that as $Bi \to \infty$ the LTNE and LTE solutions approach each other. Thus, for large numerical values of β and Bi, the average Nusselt number for the current non-Newtonian flow in porous media under LTNE should approach that of a Newtonian flow in porous media under LTE (as investigated in Ref. [5]). Tables 3 and 4 show that this is the case for a wide range of Prandtl number and permeability parameter. The contents of Fig.1 and Tables 2-4 demonstrate the validity of the conducted numerical simulations.

Also, Tables 5 and 6 demonstrate that the in the limit of large permeability and porosity of one and in the absence of diffusion of mass and gravity, the numerical solutions developed in Section 2 reduces to those of Wang [44] and Gorla [45] for stagnation flow over a cylinder. Further, although not shown in here, it was shown that for large Biot numbers the current LTNE simulations approach the LTE results of Ref. [5].

3. Results and discussion

Table 7 shows the default values of the parameters used in the simulations reported in this section. Any deviations from these values are reflected in the figure captions. In Figures 4-12, different quantities are presented over a domain that extends from $\eta = a$ to $\eta = 15$ and in which $0° \leq \varphi \leq 360°$. Furthermore, in these figures the non-uniform transpiration shown in Fig. 1 has been implemented [46-49].

3.1. Flow, temperature and concentration fields

Figure 4 depicts the effects of the Casson fluid parameter (β) on the temperature fields in the solid and fluid phases of the porous medium. It is clear from this figure that this parameter has a very strong effect upon the temperature field in the fluid phase, while the corresponding influences in the solid phase are significantly more moderate. For low values of Casson parameter, for which the fluid is substantially different from its Newtonian counterpart, the thermal boundary layer extends over the entire circumference of the cylinder. Furthermore, the thickness of the thermal boundary layer is almost uniform and the temperature distributions in the solid and fluid phases are similar, indicating the existence of LTE. However, this changes entirely as the value of the Casson parameter increases to 1 and beyond. For these values, the thermal boundary layer becomes significantly thinner for most of the circumference, while a thickening of the boundary layer is observed for $0° \lesssim \varphi \lesssim 60°$ due to the blowing of fluid.

The tendency of the porous system towards LTE at low values of the Casson fluid parameter can be explained by referring to Fig. 1, which shows that reducing the Casson fluid parameter reduces the fluid velocity. This suppresses the advection power of the heat transfer process in the porous medium and hence drives the system towards LTE. It is interesting to note that, in Fig. 4, LTE behaviour is observed for low values of β despite the fact that the value of Biot number is rather low (Bi=0.1). This shows that ,with the suppression of advection in the Casson fluid, the porous medium approaches local thermal equilibrium even for weak levels of heat exchange between the solid and fluid phases. This argument is confirmed by Fig. 5, which shows that, provided the conductivity ratio remains close to unity and for low value of β, the system remains close to LTE regardless of the value of the Biot number.

Figure 6 shows the influence of the Reynolds number on the temperature fields. Similar to that already observed, this figure indicates that the temperature of the solid phase responds slowly to changes in flow parameters. However, the temperature of the fluid phase is found to be strongly dependent upon the Reynolds number, where at low values the thermal boundary layer is thick and the porous system is under LTE. Increasing the Reynolds number results in the formation of thinner thermal boundary layers and stronger deviations from local thermal equilibrium. The physical reasons for this behaviour are, once again, related to the effects of advection upon the transport of heat in the porous medium. At low Reynolds numbers, heat advection is weak and thus for similar thermal conductivities of the fluid and solid phases the porous system is pushed towards LTE.

The influences of Damköhler and Reynolds numbers on the concentration field are investigated in Fig. 7. This figure shows that, at low values of Damköhler number and hence low catalytic activity, the concentration boundary layer is relatively thin. The effects of non-uniform transpiration are also fully noticeable in this figure. As the Damköhler number increases, the concentration boundary layer grows in thickness and intensity, and for high values of this parameter almost the entire domain is filled by the concentration boundary layer. Increasing the Reynolds number in Fig. 7b appears to have an effect similar to that discussed for Fig. 6, reducing the thickness of the concentration boundary layer. Figure 8 depicts the effects of the Schmidt and Soret numbers on the concentration fields. As expected, low values of Schmidt number yield a thicker concentration boundary layer with a region of high concentration layer near the surface. However, increasing the Schmidt number results in an almost complete elimination of this layer and also reduces the overall thickness of the concentration boundary layer. In general, depending upon the size of the molecules, the Soret number can take either positive and negative signs [41], and the effect of variations in the sign of the Soret number on the concentration field has been investigated in Fig. 8b. This figure shows that, for a fixed absolute value of Soret number, a positive sign results in a thicker concentration boundary layer. This is to be anticipated, since as shown in Eq. 7 the thermal diffusion

of mass contributes to the overall diffusion of the mass. A negative Soret number would therefore hinder the mass diffusion process, while a positive Soret number promotes it.

3.2. Entropy generation fields

The preceding sections show that, compared to the usual Newtonian fluids, the flow of the Casson fluid investigated in porous media has significantly different hydrodynamic and transport characteristics. The current section is concerned with the thermodynamic irreversibilities associated with the transport processes analysed in Section 3.1. Figure 9 shows variations in the flow and thermal entropy generation, NGF and NGT (see Eqs. 42), against changes in the Casson fluid parameter. Figure 9a indicates that the averaged frictional entropy increases significantly when the Casson parameter is reduced. As reflected in Fig. 9a, the spatial details of this increase are rather complicated. This is due partly to the complexity of the fluid under investigation and also to the convoluted nature of frictional entropy as reflected in Eq. 42. Interestingly, Fig. 9a shows that, by increasing the Casson fluid parameter and hence approaching Newtonian fluid behaviour, the complexity of frictional entropy fields decreases significantly. Part b of Fig. 9 further shows that thermal entropy is also influenced considerably by changes in the Casson parameter, where low values have resulted in weak thermal irreversibility. This behaviour can be understood in view of the earlier discussion about the tendency of the porous system to feature LTE behaviour at low values of Casson parameter. Local thermal equilibrium cancels the heat exchange between the solid and fluid and thus largely suppresses the generation of thermal entropy.

Figure 10a shows that mass transfer irreversibility is affected by changes in the value of the Casson parameter. The extent of this effect is less than that observed for frictional and thermal entropy generation (see Fig. 9) and is linked to the fact that the mass transfer process is influenced indirectly by the properties of the non-Newtonian fluid through advection and thermal diffusion effects. The variations in the Bejan number with changes in the Casson fluid parameter are depicted in Fig. 10b, indicating that a strongly non-Newtonian fluid (β=0.1) results in very small values of Bejan number. However, as a Newtonian fluid is approached, the value of the Bejan number increases considerably. This is particularly the case in the thermal and concentration boundary layers. The effects of the Brinkman number and permeability parameter upon the Bejan number for strongly non-Newtonian fluid (β=0.1) are shown in Fig. 11. A low Brinkman number and high permeability (with low values of the permeability parameter) have clearly resulted in relatively large values of Bejan number. Both effects tend to suppress the hydrodynamic stresses and thus minimise the generation of frictional entropy, which in turn magnifies the value of the Bejan number.

Figure 12 shows the effects of the Brinkman and Biot numbers on the flow and thermal entropy generation in the case of highly non-Newtonian fluid (β=0.1). It appears in Fig. 12a that increases in the Brinkman number have a strong influence on the spatial distribution of the generation of flow entropy and cause a massive increase in the magnitude of entropy generation. The Biot number, however, is comparatively inefficient in modifying the generation of thermal entropy. Figure 12b shows that increasing the Biot number by two orders of magnitude has resulted in minor changes in the entropy generation field. This is because, at low values of the Casson fluid parameter, the porous system is essentially under LTE and hence changes in Biot number does not lead to any considerable modification of the temperature field. Hence, the generation of thermal entropy remains nearly indifferent to changes in the Biot number.

3.3. Shear stress and rates of heat and mass transfer

The circumferential distribution of dimensionless shear stress applied to the surface of the cylinder is shown in Fig. 13. A common feature in this figure is that the shear stress for all investigated cases is zero at $\varphi=0$, which is the stagnation point and thus there is no shear stress. Further increases in φ result in increasing the value of dimensionless shear stress. The permeability of the porous medium and the Casson parameter have been varied, as shown in Fig. 13a. This figure shows that, as expected, increases in the permeability parameter (reducing the permeability of the porous medium) are associated with significant increases in dimensionless shear stress. This behaviour is consistent with that reported for Newtonian fluids in similar flow configurations [5]. Figure 13b indicates that the value of the Casson fluid parameter has a strongly non-linear effect upon the shear stress on the surface of the cylinder. For $\beta=0.1$, the dimensionless shear stress grows quickly. However, the rate of growth of dimensionless shear stress is substantially smaller for all other values of β investigated in Fig. 13b. Interestingly, the decrease in the numerical value of shear stress is relatively small when β is reduced from 1000 to 1. Yet, further decreases in β result in a significant increase in dimensionless stress. Table 8 provides further information on the effects of different parameters upon average shear stress.

Figure 14 shows the effects of the Biot, Dufour and Reynolds numbers and the Casson parameter on the circumferential distribution of the Nusselt number. It is clear that, in all investigated cases, for $\varphi\cong0°$ the value of the Nusselt number is very large. This is due to the formation of a stagnation point in that region and the subsequent initiation of thermal boundary layer formation (as depicted in Figs. 4-6). In keeping with the earlier discussions about the minor influence of the Biot number on the temperature field, Fig. 14a shows that the effects of the Biot number on the Nusselt number are negligible for $0°\lesssim\varphi\lesssim 60°$ and relatively small for the rest of the range. More quantitative data on averaged Nusselt numbers for different values of Biot number are provided in Table 9. These results indicate that changes in the Biot number by several orders of magnitude have only a moderate influence on the average Nusselt number. Figures 14b and 14c show that, when the Dufour and Reynolds numbers increase, the Nusselt numbers significantly decline and increase respectively. The observed negative effect of increasing the Dufour number upon the magnitude of the Nusselt number (also provided in Table 10) is in keeping with that reported in the literature [see for example [42, 43]]. In general, the strong dependency of the Nusselt number upon the Reynolds number is well-understood [41]. Figure 14c and Table 11 quantify this dependency for the non-Newtonian fluid investigated. Figure 14d and Table 12 show that increases in the Casson parameter result in major enhancements of the local and surface averaged Nusselt numbers. This is such that, by increasing the Casson parameter from 0.1 to 100, the value of the Nusselt number increases more than threefold (see Table 12). Thus, in comparison with Newtonian fluids, the investigated non-Newtonian fluid is significantly less capable of transferring heat. Table 13 shows that increases in the Prandtl number lead to major enhancements of the Nusselt number.

Figure 15 presents the variation in the Sherwood number against the pertinent parameters. Similar to the results for Nusselt number, Sherwood number appears to be highly dependent on the Reynolds number (Fig. 15a and Table 11). Figure 15b and Table 10 show that increasing the positive values of the Soret number slightly reduce the Sherwood number. However, increases in the absolute value of the negative Sort number has an inverse effect upon the Sherwood number. Figure 15c shows that the effect of the Casson parameter on the Sherwood number is similar to that on the Nusselt number. Nonetheless, as the Casson parameter increases, the Sherwood number is reduced by much less than the Nusselt number. Furthermore, Fig. 15d and Table 12 indicate that

increases in the Damköhler number and thus an intensification of the rate of heterogenous chemical reaction substantially enhance the Sherwood number. Interestingly, however, Table 12 indicates that the augmentation of the Damköhler number reduces the Nusselt number. This behaviour can be explained by noting the connection between species transport and the thermal field thorough the Dufour number, as it has been shown that enhancements of the Dufour number reduce the Nusselt number. Finally, the Schmitt number appears to have a positive correlation with the average Sherwood number (see Table 13), although this is less pronounced than the correlation between the Prandtl number and the average Nusselt number.

4. Conclusions

The combined transport of heat and chemical species in the stagnation-point flow of Casson fluid over a cylinder covered by a layer of catalyst and embedded in a porous medium was investigated. The non-equilibrium thermodynamics of the problem were taken into account. These include Soret and Dufour effects in the transport of heat and mass, as well as local thermal non-equilibrium in the porous medium. Furthermore, circumferentially non-uniform transpiration of fluid was imposed on the external surface of the cylinder. The governing equations were first reduced to non-linear ordinary differential equations through the introduction of similarity variables, and a finite-difference scheme was then employed to solve the resulting system of equations. The key findings of this work can be summarised as follows.

- For low values of the Casson parameter and thus strong non-Newtonian behaviour of the fluid, the investigated porous system featured LTE for a wide range of Biot number. This was attributed to the suppression of fluid motion (advection) at low values of the Casson parameter which, for values of conductivity ratio close to unity, maintain local thermal equilibrium.
- Non-uniform transpiration appeared to have a strong influence upon the temperature, concentration and irreversibility fields. It is therefore concluded that non-uniform transpiration is a strongly influential factor in the investigated problem.
- The Casson fluid showed far more complex behaviour in frictional entropy generation in comparison with the corresponding Newtonian fluid.
- Increases in the Casson parameter enhance the value of the Bejan number considerably through the suppression of frictional entropy, reflecting the importance of deviation from the Newtonian fluid behaviour.
- Lowering the value of the Casson parameter was observed to significantly reduce the Nusselt number and to a lesser extent decrease the value of the Sherwood number.

To the best of the present author's knowledge this is the first study of the stagnation-point flow of Casson fluids in curved porous configurations and complemented the recent results on Casson fluid flows through porous media in other configurations [49, 50, 51].

Additional Information:

Competing Interests: The authors declare no competing interests.

References

1. K. Vafai, Handbook of porous media, CRC Press (2015).

2. R.P. Chhabra, J.F. Richardson, Non-Newtonian flow and applied rheology: engineering applications, Butterworth-Heinemann (2011).
3. M. Doi, Soft matter physics, Oxford University Press (2013).
4. S.S. Feng, J.J. Kuang, T. Wen, T.J. Lu, K. Ichimiya, An experimental and numerical study of finned metal foam heat sinks under impinging air jet cooling, Int. J. Heat Mass Transf. 77 (2014) 1063-1074.
5. R. Alizadeh, A.B. Rahimi, N. Karimi, A. Alizadeh, On the Hydrodynamics and Heat convection of an Impinging External Flow upon a cylinder with Transpiration and Embedded in a Porous Medium, Transp Porous Med. 120 (2017) 579-604.
6. B. Buonomo, G. Lauriat, O. Manca, S. Nardini, Numerical investigation on laminar slot-jet impinging in a confined porous medium in local thermal non-equilibrium, Int. J. Heat Mass Transf. 98 (2016) 484-492.
7. M. Mustafa, T. Hayat, P. Ioan, A. Hendi, Stagnation-point flow and heat transfer of a Casson fluid towards a stretching sheet, Z Naturforsch A. 67 (2012) 70-76.
8. T. Hayat, S.A. Shehzad, A. Alsaedi, Soret and Dufour effects on magnetohydrodynamic (MHD) flow of Casson fluid, Appl. Math. Mech. 33 (2012) 1301-1312.
9. M.Y. Malik, M. Naseer, S. Nadeem, A. Rehman, The boundary layer flow of Casson nanofluid over a vertical exponentially stretching cylinder, Appl. Nanosci. 4 (2014) 869-873.
10. S. Nadeem, R.u. Haq, N.S. Akbar, MHD three-dimensional boundary layer flow of Casson nanofluid past a linearly stretching sheet with convective boundary condition, IEEE Trans. Nanotechnol. 13 (2014) 109-115.
11. M.H. Abolbashari, N. Freidoonimehr, F. Nazari, M.M. Rashidi, Analytical modeling of entropy generation for Casson nano-fluid flow induced by a stretching surface, Adv Powder Technol. 26 (2015) 542-552.
12. A. Khalid, I. Khan, A. Khan, S. Shafie, Unsteady MHD free convection flow of Casson fluid past over an oscillating vertical plate embedded in a porous medium, Eng. Sci. Technol. Int J. 18 (2015) 309-317.
13. Z. Abbas, M. Sheikh, S.S. Motsa, Numerical solution of binary chemical reaction on stagnation point flow of Casson fluid over a stretching/shrinking sheet with thermal radiation, Energy 95 (2016) 12-20.
14. A.A. Hakeem, P. Renuka, N.V. Ganesh, R. Kalaivanan, B. Ganga, Influence of inclined Lorentz forces on boundary layer flow of Casson fluid over an impermeable stretching sheet with heat transfer, J. Magn. Magn. Mater. 401 (2016) 354-361.
15. A. Rauf, M.K. Siddiq, F.M. Abbasi, M.A. Meraj, M. Ashraf, S.A. Shehzad, Influence of convective conditions on three dimensional mixed convective hydromagnetic boundary layer flow of Casson nanofluid, J. Magn. Magn. Mater. 416 (2016) 200-207.
16. M.I. Khan, M. Waqas, T. Hayat, A. Alsaedi, A comparative study of Casson fluid with homogeneous-heterogeneous reactions, J. Colloid Interface Sci. 498 (2017) 85-90.
17. G.K. Ramesh, K.G. Kumar, S.A Shehzad, B.J. Gireesha, Enhancement of radiation on hydromagnetic Casson fluid flow towards a stretched cylinder with suspension of liquid-particles, Can. J. Phys. 999 (2017) 18-24.
18. S. Rana, R. Mehmood, N.S. Akbar, Mixed convective oblique flow of a Casson fluid with partial slip, internal heating and homogeneous–heterogeneous reactions, J Mol Liq. 222 (2016) 1010-1019.

19. K.U. Rehman, M.Y. Malik, M. Zahri, M. Tahir, Numerical analysis of MHD Casson Navier's slip nanofluid flow yield by rigid rotating dis, Results Phys. 8 (2018) 744-751.
20. L. Govone, M. Torabi, G. Hunt, N. Karimi, N. Non-equilibrium thermodynamic analysis of double diffusive, nanofluid forced convection in catalytic microreactors with radiation effects, Entropy 19 (2017) 690.
21. L. Govone, M. Torabi, L. Wang, N. Karimi, Effects of nanofluid and radiative heat transfer on the double diffusive forced convection in microreactors, J Therm Anal Calorim. 135 (2018) 45-59.
22. G. Hunt, N. Karimi, M. Torabi, Two-dimensional analytical investigation of coupled heat and mass transfer and entropy generation in a porous catalytic microreactor, Int. J. Heat Mass Transf. 119 (2018) 372-391.
23. G. Hunt, M. Torabi, L. Govone, N. Karimi, A. Mehdizadeh, Two-dimensional heat and mass transfer and thermodynamic analyses of porous microreactors with Soret and thermal radiation effects-An analytical approach, Chem Eng Process. 126 (2018) 190-205.
24. N. Sandeep, O.K. Koriko, I.L. Animasaun, Modified kinematic viscosity model for 3D-Casson fluid flow within boundary layer formed on a surface at absolute zero, J Mol Liq. 221 (2016) 1197-1206.
25. R. Alizadeh, A.B. Rahimi, M. Najafi, Unaxisymmetric stagnation-point flow and heat transfer of a viscous fluid on a moving cylinder with time-dependent axial velocity, J Braz Soc Mech Sci Eng. 38 (2016) 85-98.
26. R. Alizadeh, A.B. Rahimi, R. Arjmandzadeh, M. Najafi, A. Alizadeh, Unaxisymmetric stagnation-point flow and heat transfer of a viscous fluid with variable viscosity on a cylinder in constant heat flux, Alexandria Eng J. 55 (2016) 1271-1283.
27. R. Alizadeh, A.B. Rahimi, M. Najafi, Magnetohydrodynamic unaxisymmetric stagnation-point flow and heat transfer of a viscous fluid on a stationary cylinder, Alexandria Eng J. 55 (2016) 37-49.
28. Alizadeh, Rasool, Nader Karimi, and Amireh Nourbakhsh. "Effects of radiation and magnetic field on mixed convection stagnation-point flow over a cylinder in a porous medium under local thermal non-equilibrium." Journal of Thermal Analysis and Calorimetry (2019): 1-21.
29. Alizadeh, R., Karimi, N., Mehdizadeh, A., & Nourbakhsh, A. (2019). Analysis of transport from cylindrical surfaces subject to catalytic reactions and non-uniform impinging flows in porous media. Journal of Thermal Analysis and Calorimetry, 1-20.
30. Alizadeh, R., Rahimi, A. B., Karimi, N., & Alizadeh, A. (2018). Transient analysis of the interactions between a heat transferring, radial stagnation flow, and a rotating cylinder-magnetohydrodynamic and nonuniform transpiration effects. Journal of Thermal Science and Engineering Applications, 10(5), 051017.
31. Gomari, S. R., Alizadeh, R., Alizadeh, A., & Karimi, N. (2019). Generation of entropy during forced convection of heat in nanofluid stagnation-point flows over a cylinder embedded in porous media. Numerical Heat Transfer, Part A: Applications, 75(10), 647-673.
32. M. Torabi, N. Karimi, K. Zhang, Heat transfer and second law analyses of forced convection in a channel partially filled by porous media and featuring internal heat sources, Energy 93(2015) 106-127.
33. N. Karimi, D. Agbo, A.T. Khan, P.L. Younger, On the effects of exothermicity and endothermicity upon the temperature fields in a partially-filled porous channel, Int. J. Therm. Sci. 96 (2015) 128-148.

34. R. Alizadeh, N. Karimi, R. Arjmandzadeh, A. Mehdizadeh, Mixed convection and thermodynamic irreversibilities in MHD nanofluid stagnation-point flows over a cylinder embedded in porous media, J Therm Anal Calorim. (2018) 489-506.
35. R. Saleh, A.B. Rahimi, Axisymmetric Stagnation-Point Flow and Heat Transfer of a Viscous Fluid on a Moving Cylinder with Time- Dependent Axial Velocity and Uniform Transpiration, J. Fluids Eng. 126 (2004) 997-1005.
36. J.W. Thomas, Numerical partial differential equations: finite difference methods, New York: Springer Science & Business Media 22 (2013).
37. P. Ganesan, G. Palani, Finite difference analysis of unsteady natural convection MHD flow past an inclined plate with variable surface heat and mass flux, Int. J. Heat Mass Transf. 47 (2004) 4449-4457.
38. M. Torabi, N. Karimi, G.P. Peterson, S. Yee, Challenges and progress on modeling of entropy generation in porous media: A review, Int. J. Heat Mass Transf. 114 (2017) 31-46.
39. M. Torabi, K. Zhang, N. Karimi, G.P. Peterson, Entropy generation in thermal systems with solid structures-a concise review. Int. J. Heat Mass Transf. 97 (2016) 917-931.
40. G.R. Kefayati, Simulation of double diffusive natural convection and entropy generation of power-law fluids in an inclined porous cavity with Soret and Dufour effects (Part II: Entropy generation), Int. J. Heat Mass Transf. 94 (2016) 582-624.
41. W.M. Deen, Analysis of Transport Phenomena, Topics in Chemical Engineering, New York: Oxford University Press, 2 (1998).
42. S.Z.A. Zaidi, S.T. Mohyud-Din, Analysis of wall jet flow for Soret, Dufour and chemical reaction effects in the presence of MHD with uniform suction/injection, Appl. Therm. Eng. 103 (2016) 971-979.
43. M.K. Partha, P.V.S.N. Murthy, G.R Sekhar, Soret and Dufour effects in a non-Darcy porous medium. J. Heat Transfer 128 (2006) 605-610.
44. C.Y. Wang, Axisymmetric stagnation flow on a cylinder, Q Appl Math. 32(1974) 207–13.
45. R.S.R. Gorla, Heat transfer in an axisymmetric stagnation flow on a cylinder, Appl Sci Res. 32(1976) 541–53.
46. M. Siavashi, K. Karimi, Q. Xiong, M.H. Doranehgard, Numerical analysis of mixed convection of two-phase non-Newtonian nanofluid flow inside a partially porous square enclosure with a rotating cylinder, J Therm Anal Calorim. 137(2019) 267-87.
47. A. Izadi, M. Siavashi, Q. Xiong, Impingement jet hydrogen, air and CuH2O nanofluid cooling of a hot surface covered by porous media with non-uniform input jet velocity, Int. J. Hydrogen Energy 44(2019) 15933-48.
48. M.V. Bozorg, M.H. Doranehgard, K. Hong, Q. Xiong, CFD study of heat transfer and fluid flow in a parabolic trough solar receiver with internal annular porous structure and synthetic oil–Al2O3 nanofluid, Renewable Energy 145(2020) 2598-2614.
49. Q. Xiong, S.C. Kong, High-resolution particle-scale simulation of biomass pyrolysis, ACS Sustainable Chem. Eng. 4(2016) 5456-61.
50. A. Saeed, N. Karimi, G. Hunt, M. Torabi, On the influence of surface heat release and thermal radiation upon transport in catalytic porous microreactors-A novel porous-solid interface model, Chemical Engineering and Processing-Process Intensification, 143 (2019), 107602.

51. A. Saeed, N. Karimi, G. Hunt, M. Torabi, A. Mehdizadeh, Double-diffusive transport and thermodynamic analysis of a magnetic microreactor with non-Newtonian biofluid flow, Journal of Thermal Analysis and Calorimetry, 2019, DOI: 10.1007/s10973-019-08415-1.

Figures

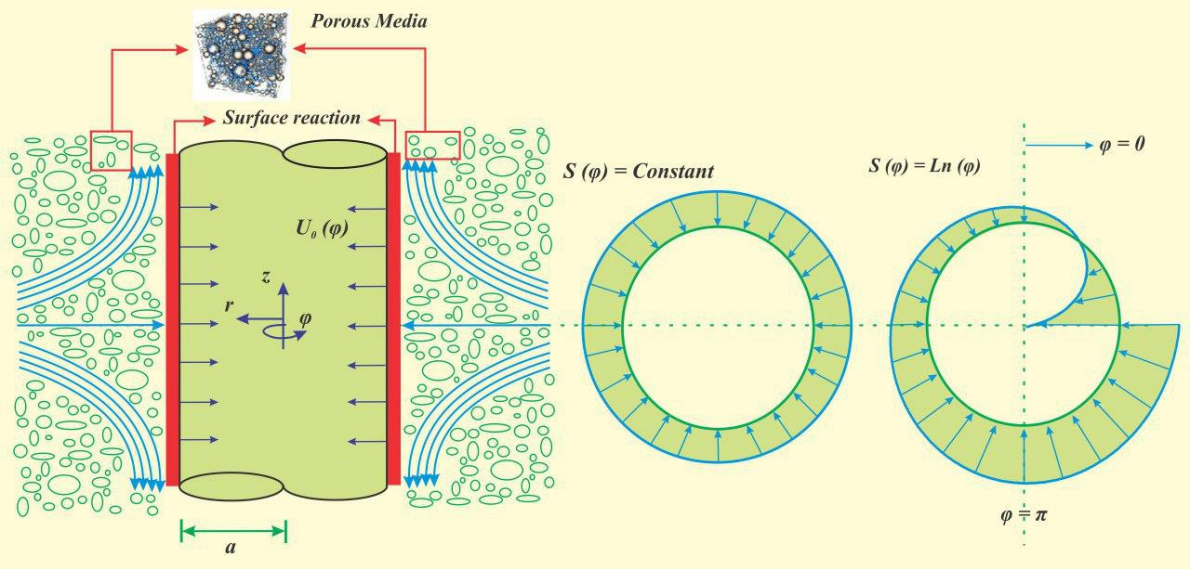

Fig. 1 Schematic view of a stationary cylinder under radial stagnation flow in porous media grid system

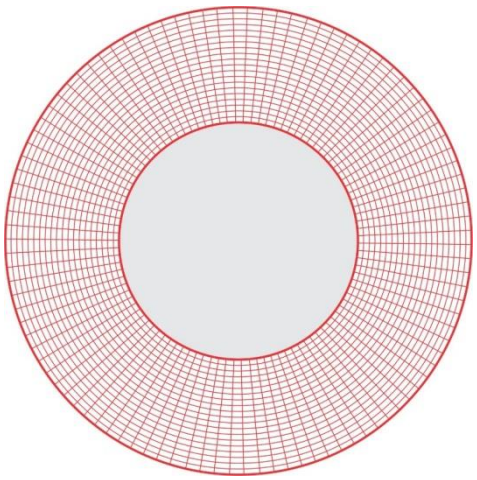

Fig. 2 Sample of grid system

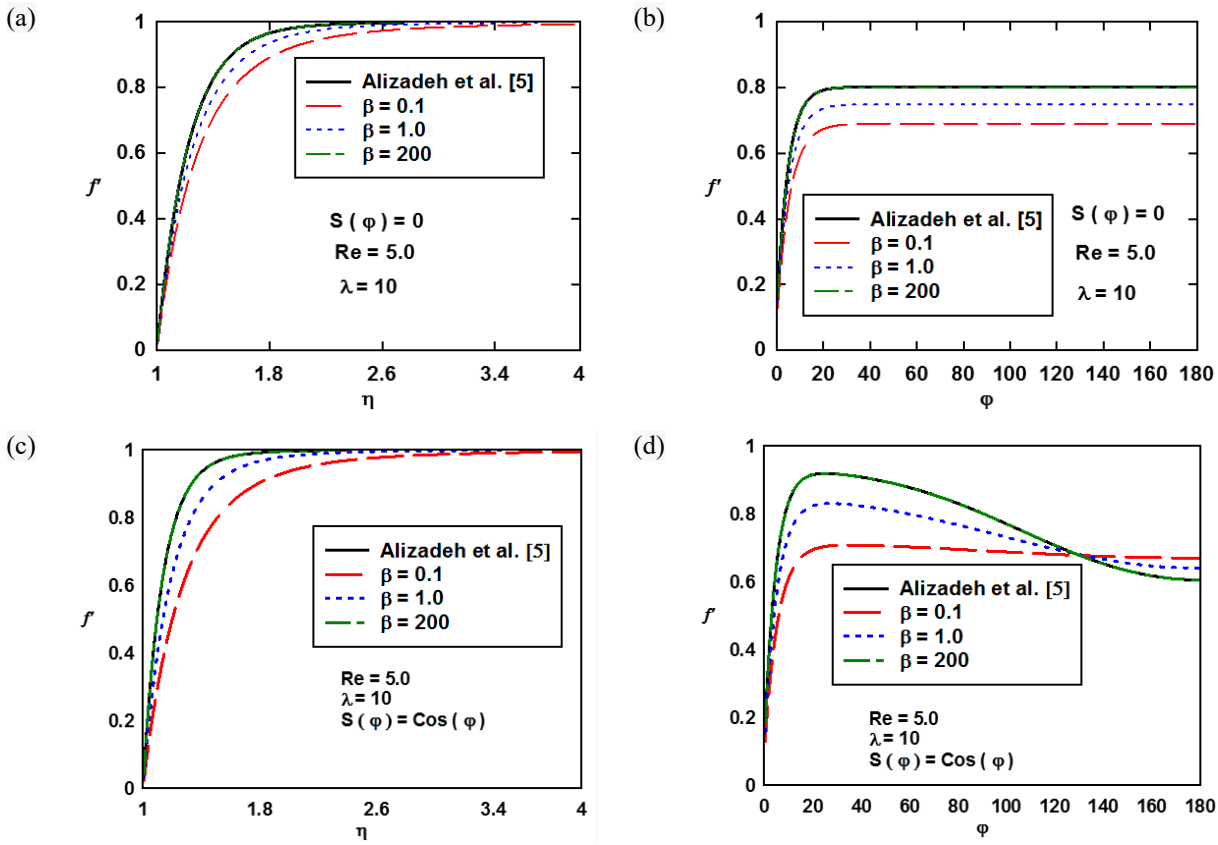

Fig. 3. Comparison between the $\acute{f}(\eta, \varphi)$ in the current work and those of Alizadeh et al. [5] in terms of (a) η (radial),(b) φ (angular) $Df = 0, Bi = 1000, Sr = 0, Re = 5, \lambda = 10$ and for different values of the Casson fluid parameter

(a) **(b)**

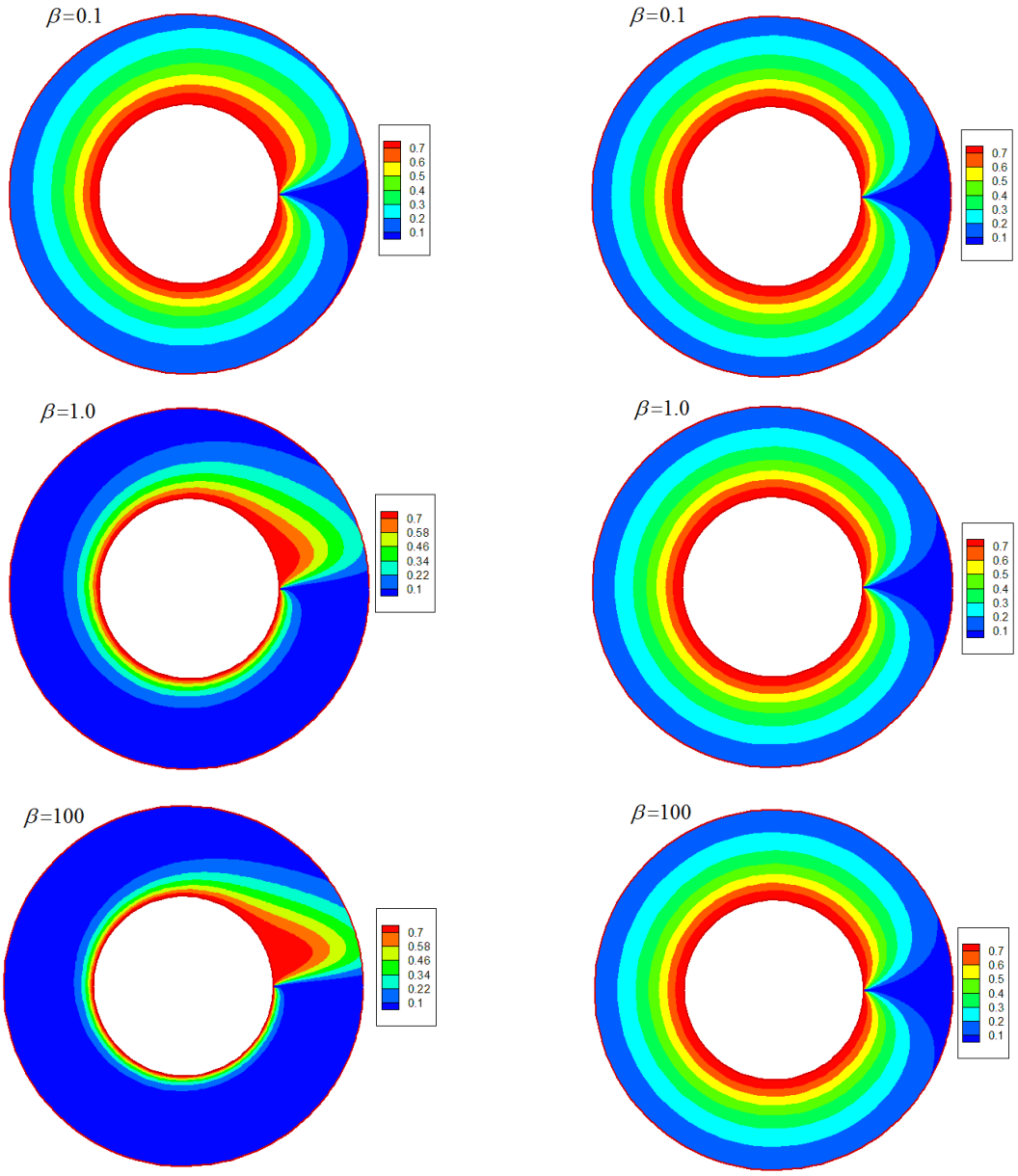

Fig. 4. Effects of Casson fluid parameter on (a) distribution of $\theta_f(\eta,\varphi)$, (b) distribution of $\theta_s(\eta,\varphi)$, $Df = 1.0$, $Sr = 0.5$, $Sc = 0.1$, $Re = 10$, $Bi = 0.1$, $\lambda = 10$, $\gamma = 1.5$

(a) **(b)**

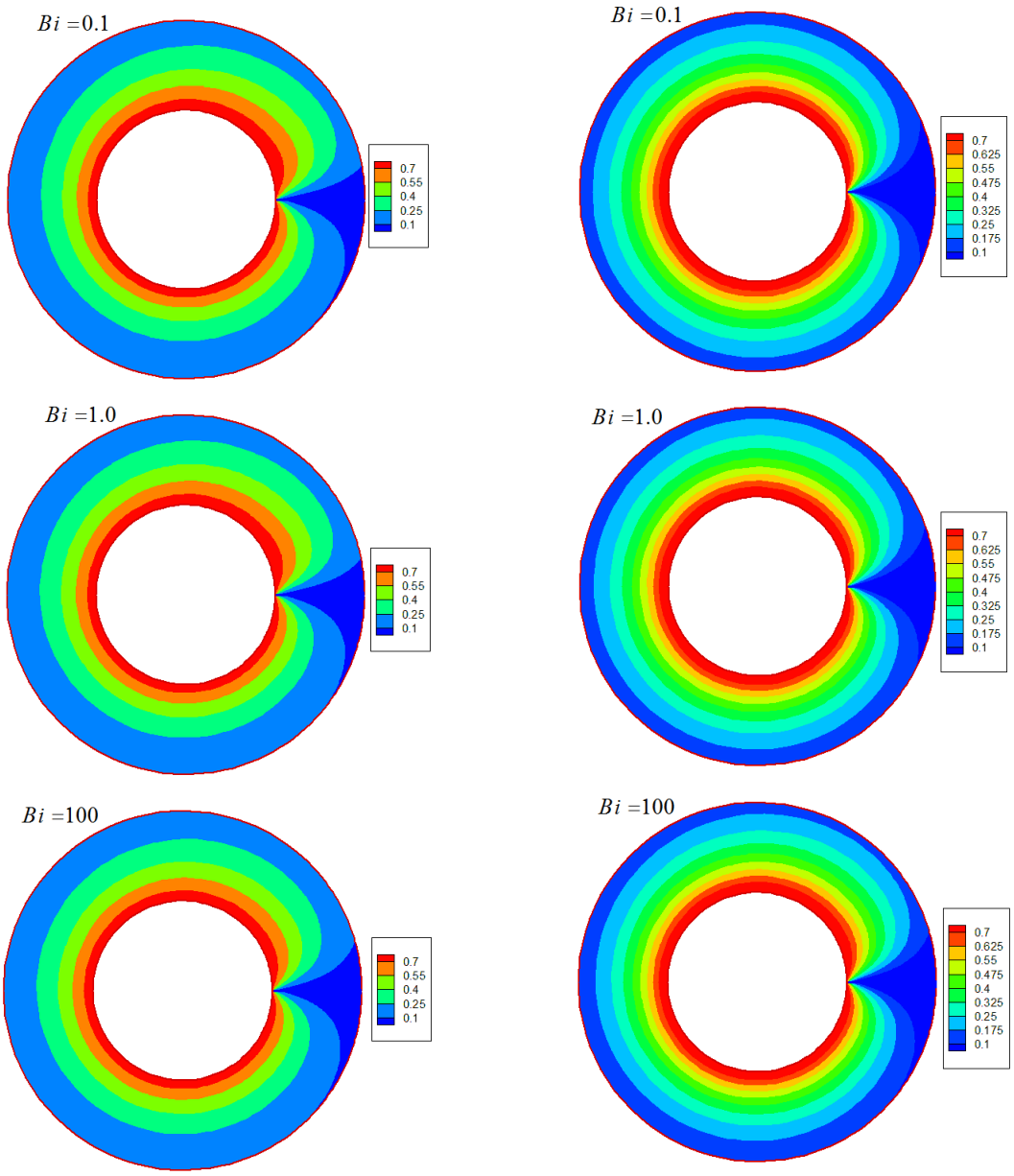

Fig. 5. Effects of Biot number on (a) distribution of $\theta_f(\eta,\varphi)$, (b) distribution of $\theta_s(\eta,\varphi)$

$Df = 1.0\,, Sr = 0.5\,, Sc = 0.1\,, Re = 10\,, \lambda = 10\,\,, \gamma = 1.5\,, \gamma^* = 1.0\,, \beta = 0.1$

(a) **(b)**

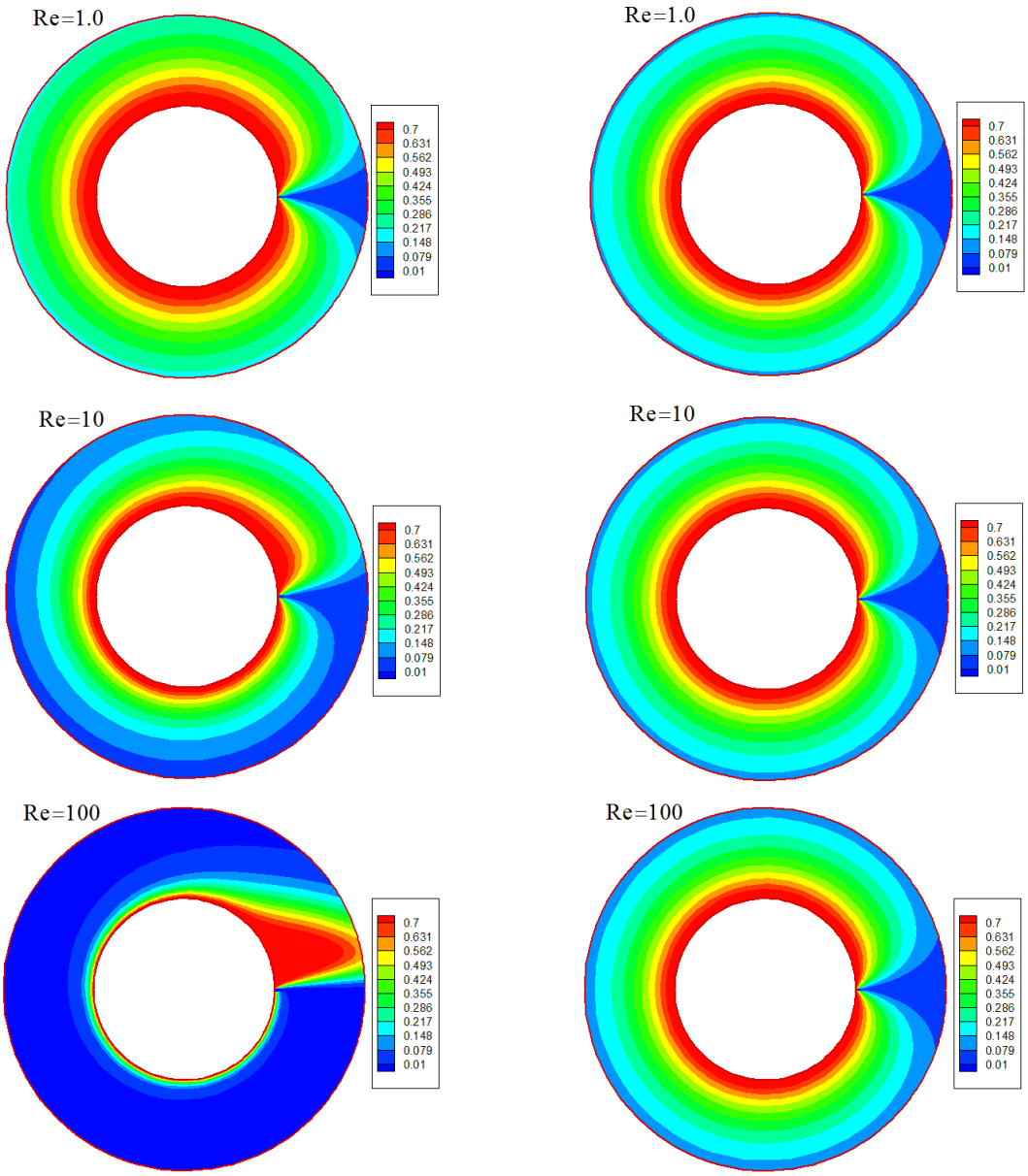

Fig. 6. Effects of Reynolds number on (a) distribution of $\theta_f(\eta,\varphi)$, (b) distribution of $\theta_s(\eta,\varphi)$, $Df = 1.0$, $Sr = 0.5$, $Sc = 0.1$, $Bi = 0.1$, $\lambda = 10$, $\gamma = 1.5$, $\gamma^* = 1.0$, $\beta = 0.1$

a) **(b)**

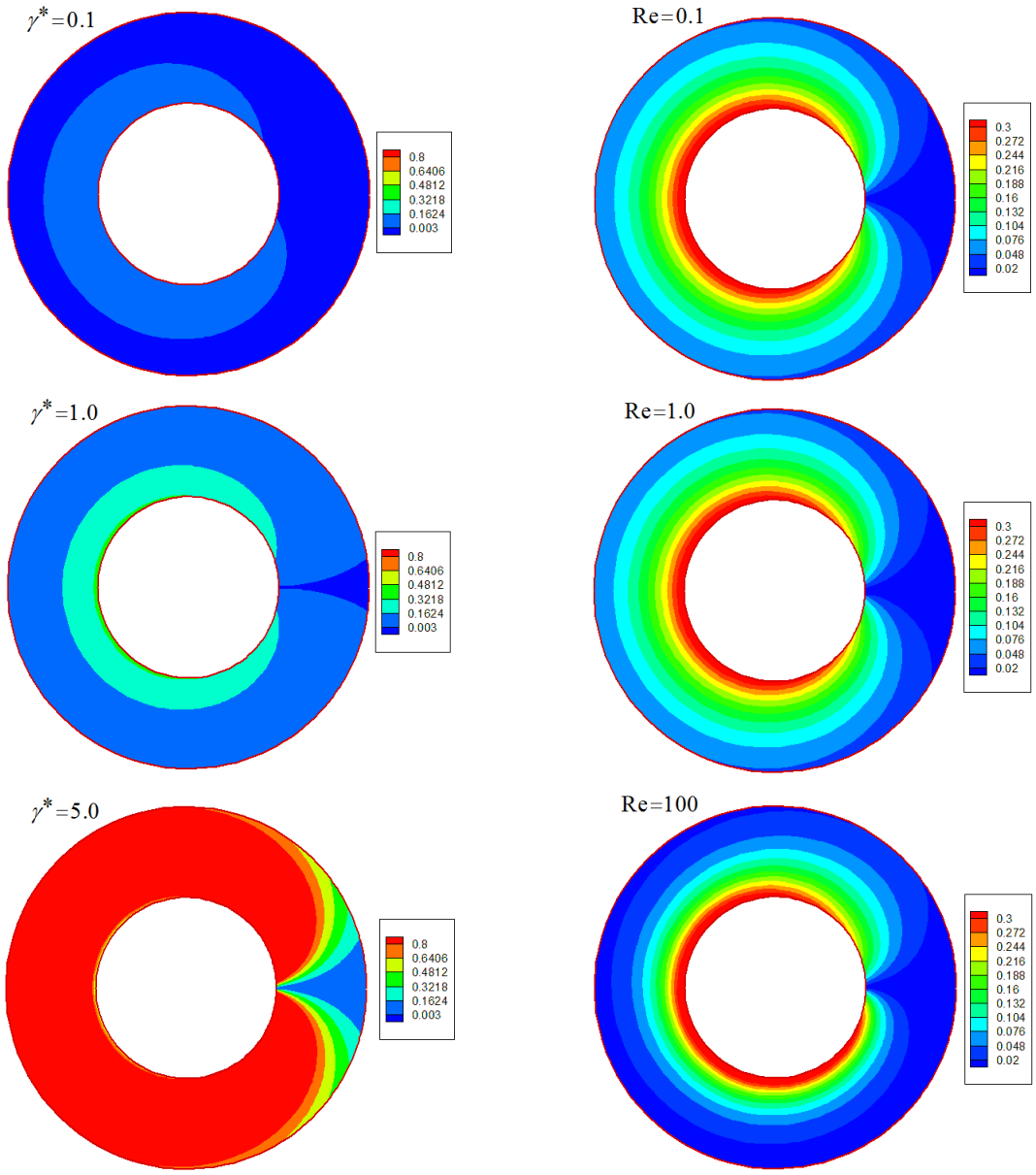

Fig. 7. Variation of $\phi(\eta, \varphi)$ for different values of (a) Damköhler number (γ^*) , (b) Reynolds number (Re), $Df = 1.0$, $Sr = 0.5$, $Sc = 0.1$, $Re = 10$, $Bi = 0.1$, $\lambda = 10$, $\gamma = 1.5$, $\gamma^* = 1.0$, $\beta = 0.1$

(a) **(b)**

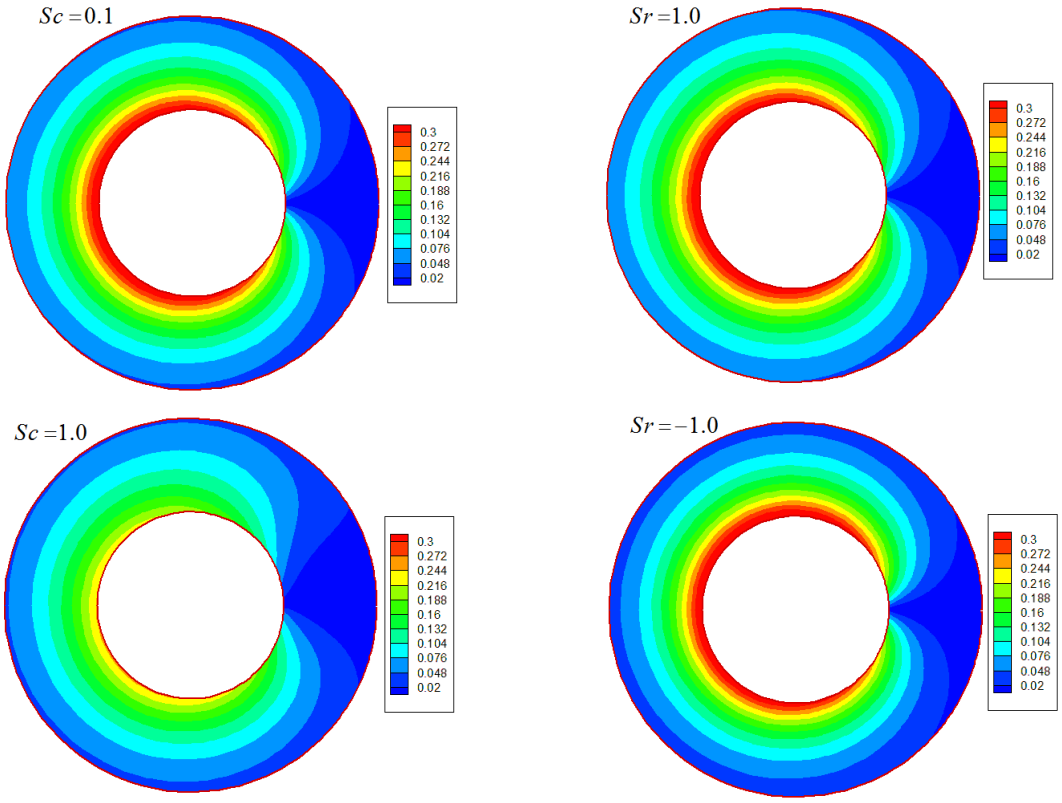

Fig. 8. Variation of $\phi(\eta,\varphi)$ for different values of (a) Schmidt number (Sc) , (b) Soret number (Sr), $Df = 1.0\,, Sr = 0.5\,, Sc = 0.1\,, Re = 10\,, Bi = 0.1\,, \lambda = 10\,\,, \gamma = 1.5\,, \gamma^* = 1.0\,, \beta = 0.1$

(a) **(b)**

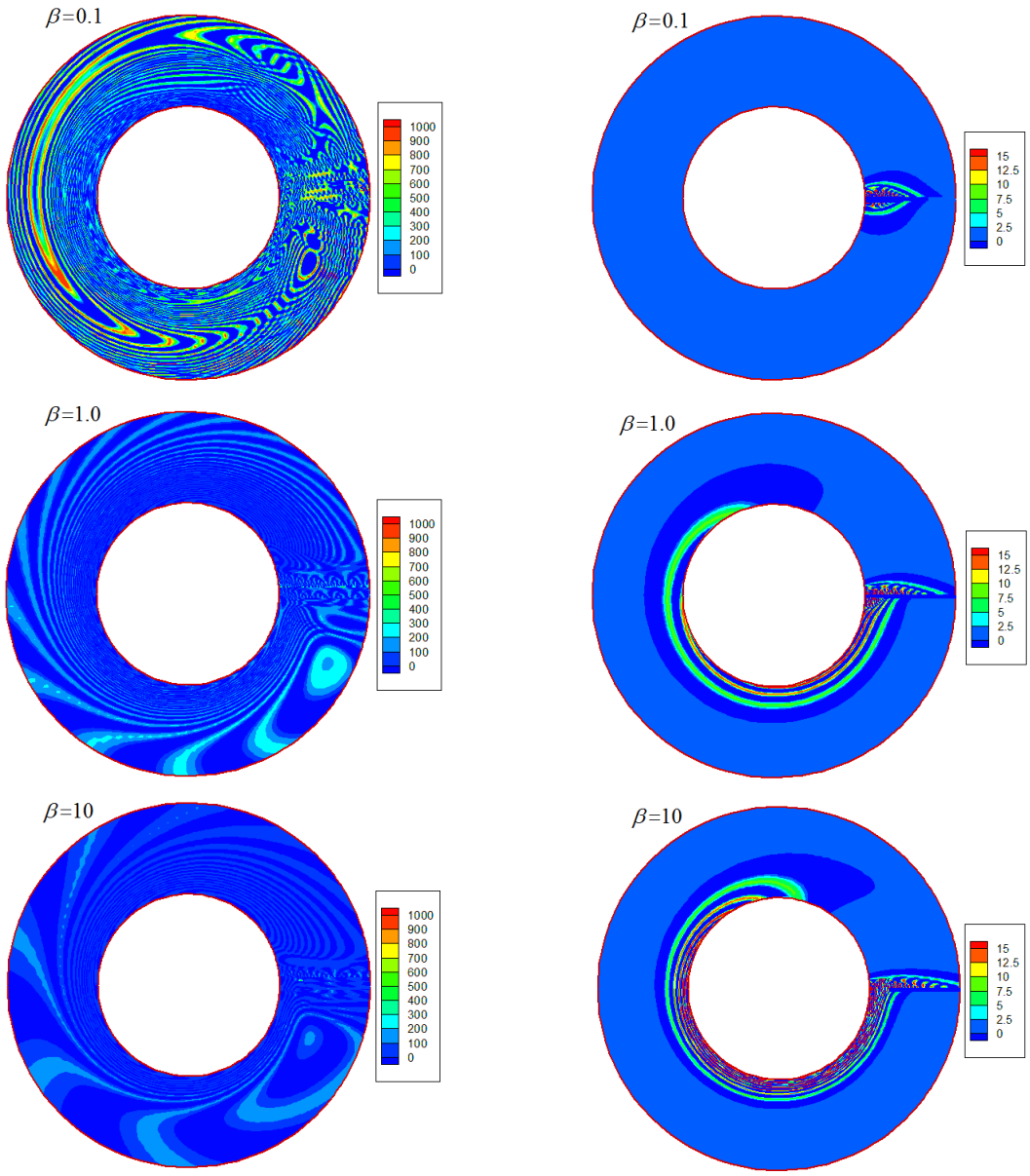

Fig. 9. Effects of Casson fluid parameter on (a) distribution of $N_{GF}(\eta,\varphi)$, (b) distribution of $N_{GT}(\eta,\varphi)$, $Df = 1.0$, $Sr = 0.5$, $Sc = 0.1$, $Re = 10$, $Bi = 0.1$, $\lambda = 10$, $\gamma = 1.5$, $\gamma^* = 1.0$, $\Lambda = 1.0$, $\mathrm{Br} = 2.0$.

(a) **(b)**

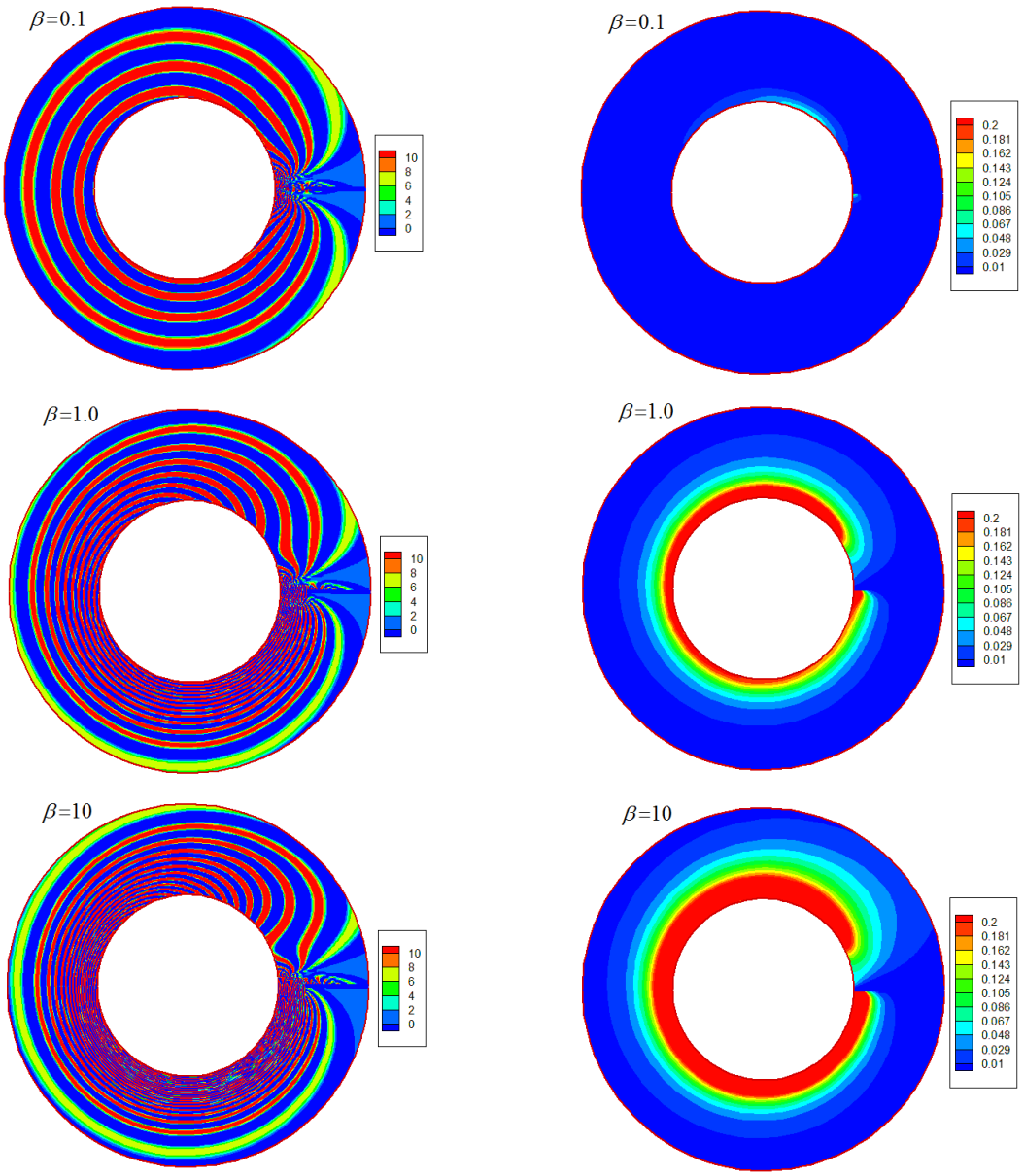

Fig. 10. Effects of Casson fluid parameter on (a) distribution of $N_{GD}(\eta,\varphi)$,(b) distribution of $Be(\eta,\varphi)$, $Df = 1.0$, $Sr = 0.5$, $Sc = 0.1$, $Re = 10$, $Bi = 0.1$, $\lambda = 10$, $\gamma = 1.5$, $\gamma^* = 1.0$, $\Lambda = 1.0$, $\mathrm{Br} = 2.0$.

(a) **(b)**

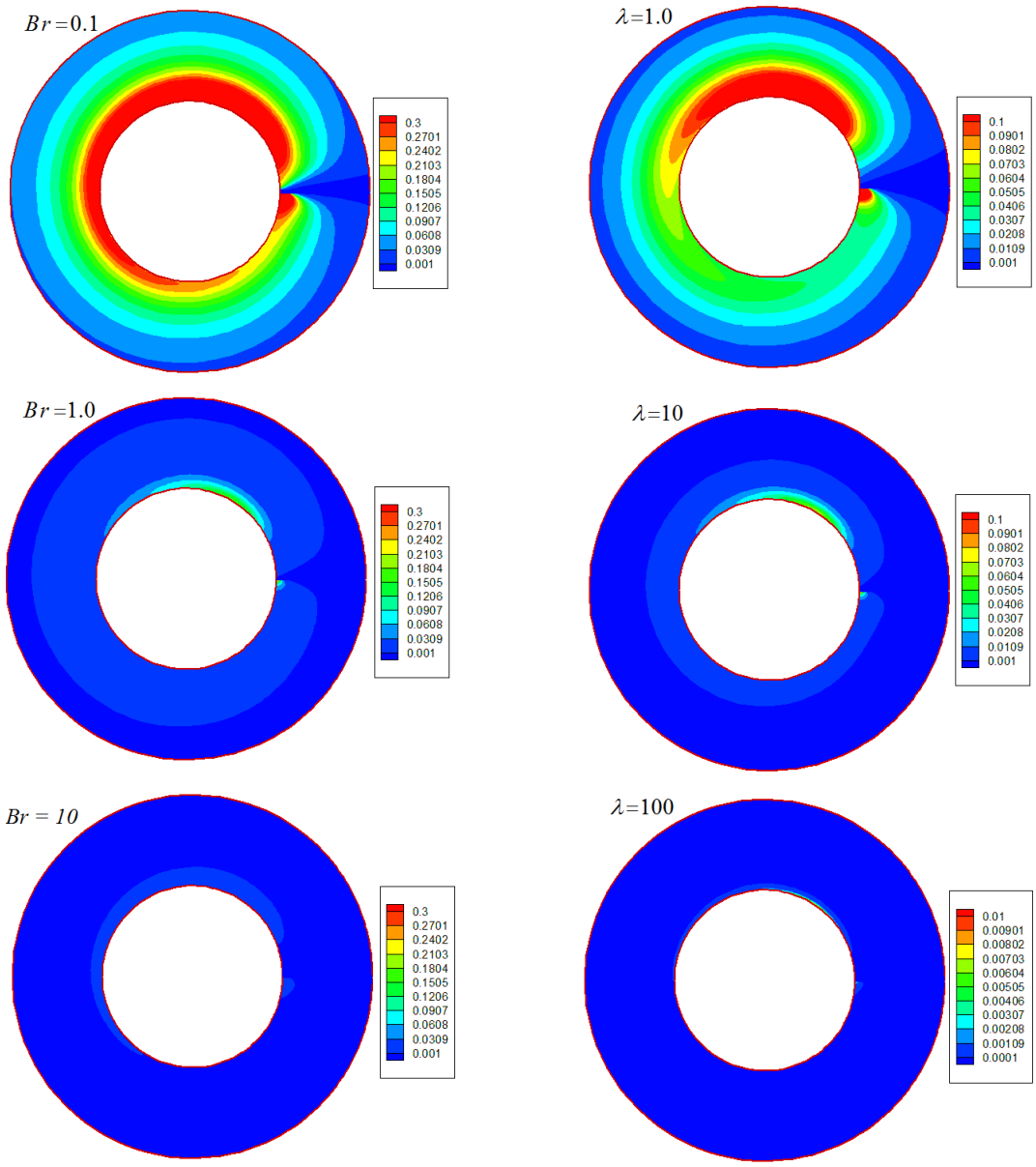

Fig.11. Variation of $B(\eta, \varphi)$ for different values of (a) Brinkman number (Br) , (b) Permeability parameter (λ), $Df = 1.0$, $Sr = 0.5$, $Sc = 0.1$, $Re = 10$, $Bi = 0.1$, $\lambda = 10$, $\gamma = 1.5$, $\gamma^* = 1.0$, $\beta = 0.1, \Lambda = 1$, $Br = 2.0$

a) **(b)**

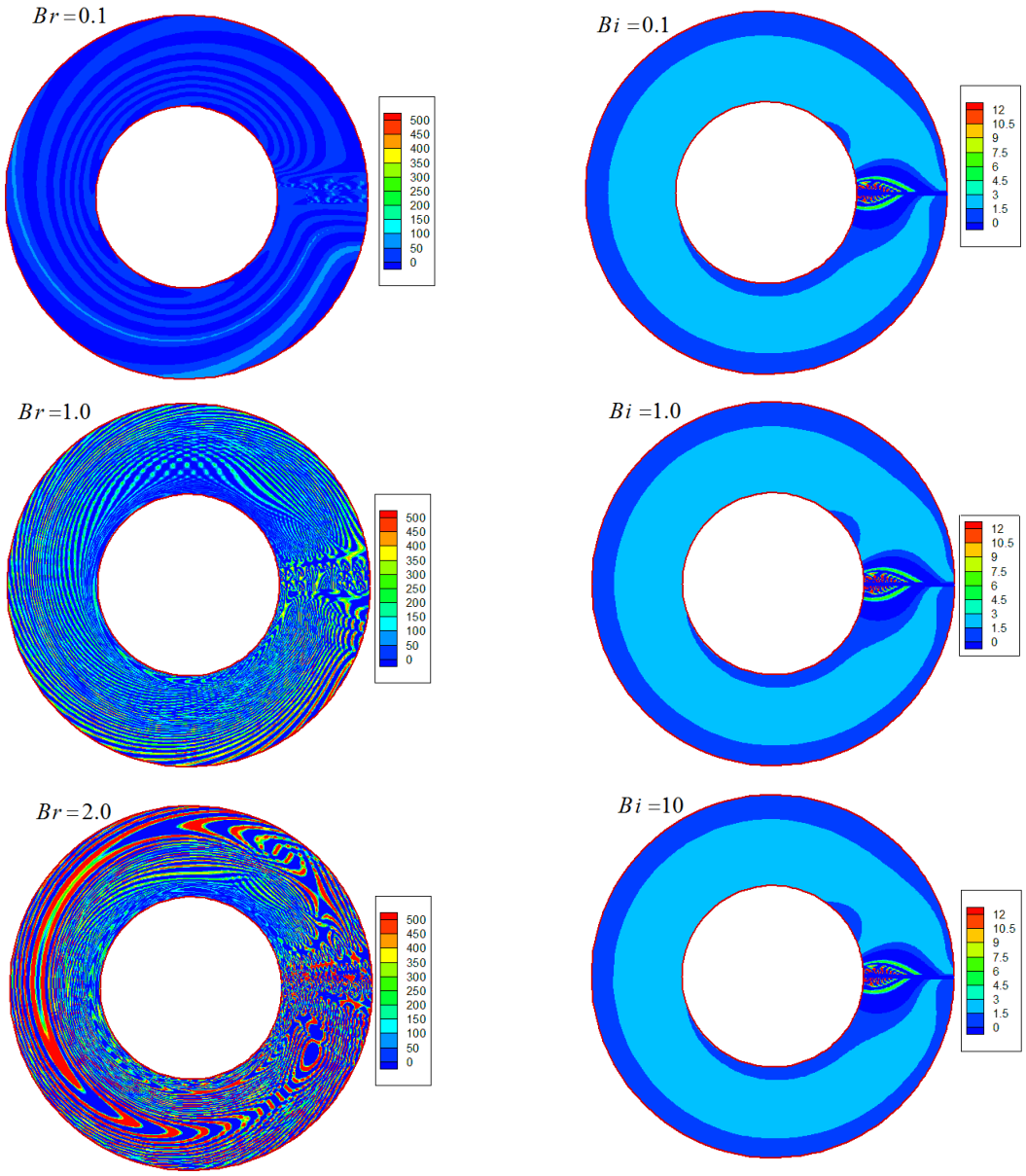

Fig. 12. (a) Effects of Brinkman number on $N_{GF}(\eta, \varphi)$,(b) Effects of Biot number on $N_{GT}(\eta, \varphi)$, $Df = 1.0$, $Sr = 0.5$, $Sc = 0.1$, $Re = 10$, $Bi = 0.1$, $\lambda = 10$, $\gamma = 1.5$, $\gamma^* = 1.0$, $\beta = 0.1$, $\mathrm{Br} = 2.0$

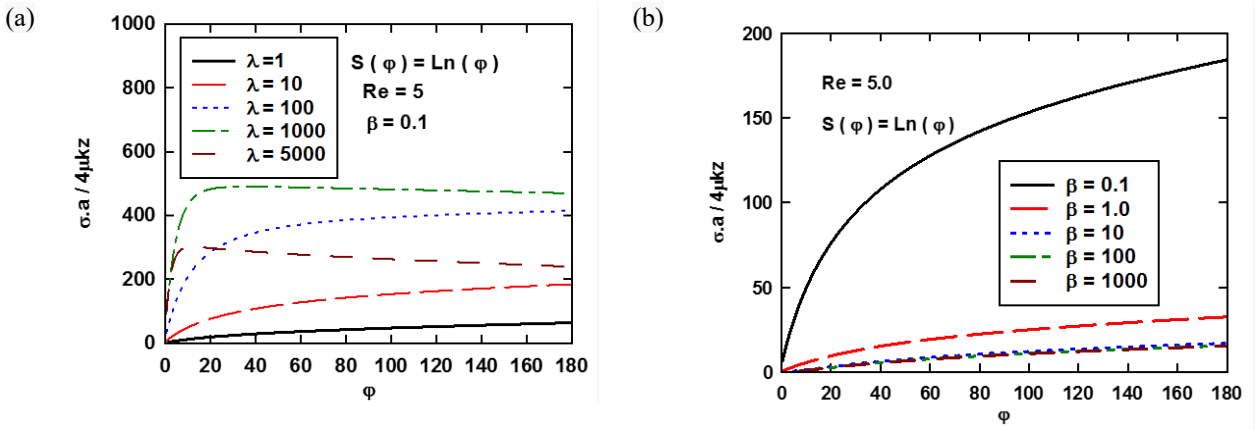

Fig. 13. Variation of $\frac{\sigma_m.a}{4\mu kz}$ for different values of (a) Permeability parameter (λ) ,(b) Casson fluid parameter (β) , $Re = 5.0$, $\lambda = 10$, $\beta = 0.1$

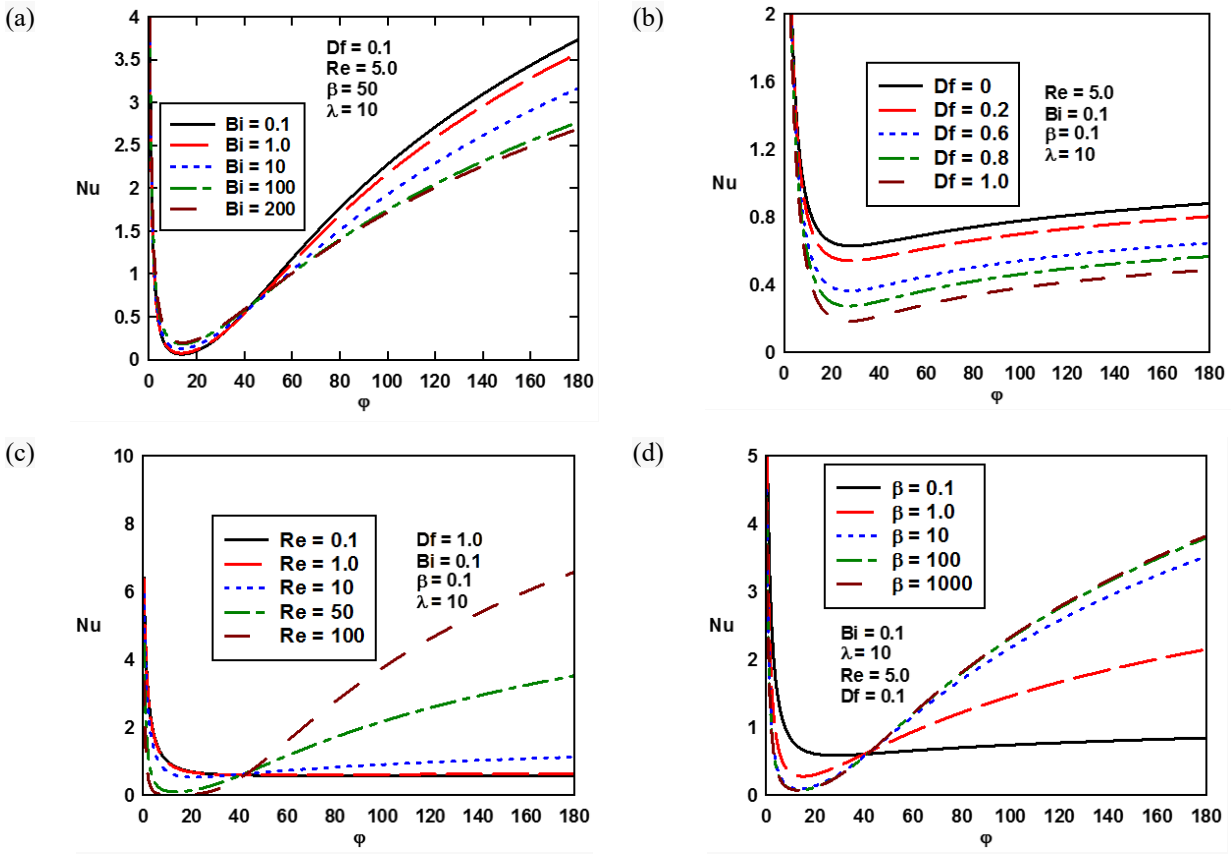

Fig. 14. Variation of Nu for different values of (a) Biot number (Bi),(b) Dufour number (Df), (c) Reynolds number (Re),(d) Casson fluid parameter (β), $Df = 1.0$, $Re = 5.0$, $Bi = 0.1$, $\gamma = 1.5$, $\lambda = 10$.

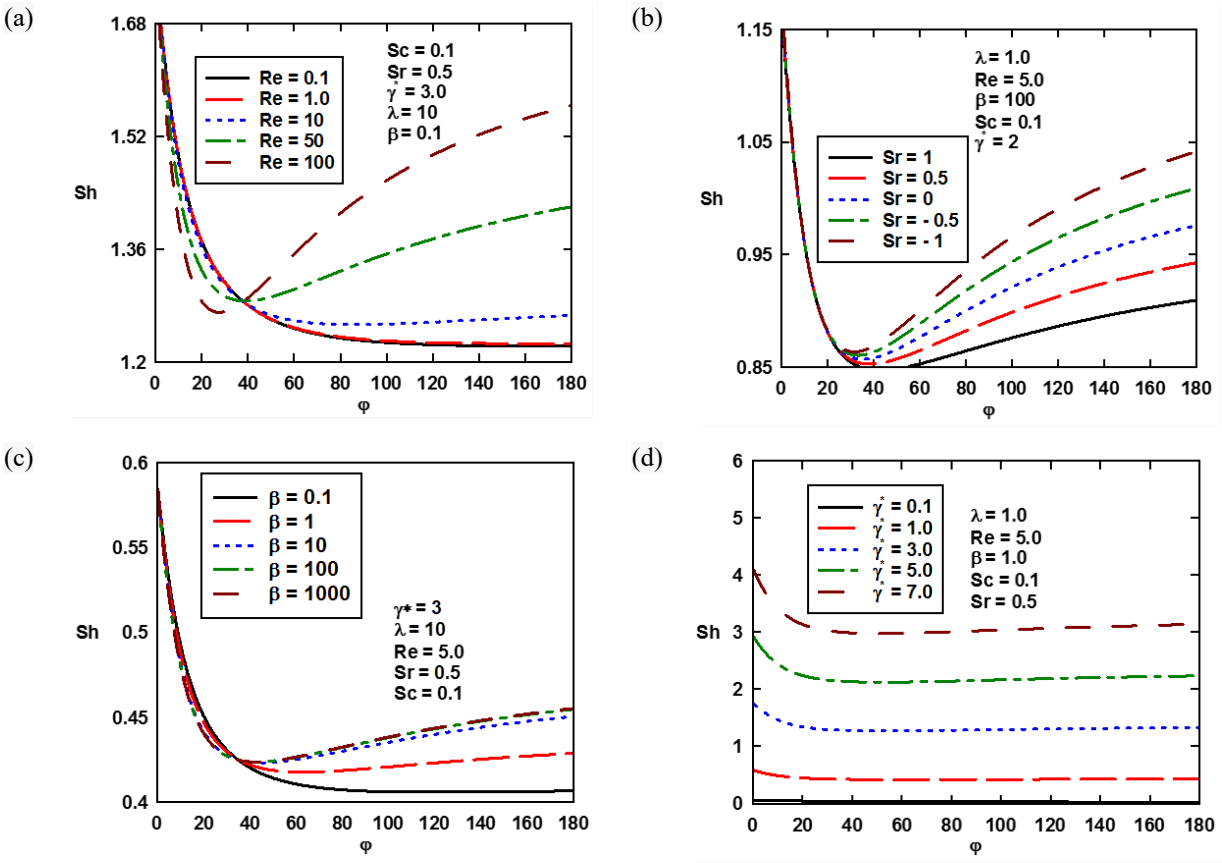

Fig. 15. Variation of Sh for different values of (a) Reynolds number (Re),(b) Soret number (Sr), (c) Permeability parameter (λ) , (d) Damköhler number (γ^*), Df $= 1.0$, Re $= 5.0$, Bi $= 0.1$, $\gamma = 1.5$, $\lambda = 10$, Sc $= 0.1$, $\gamma^* = 2.0$, Sr $= 0.5$.

Tables

Table 1. Grid independence study at $Df = 0.1$, $\beta = 100$, $Sr = 0.5$, $Re = 10$, $Sc = 0.1$, $\lambda = 10$, $\gamma^* = 3.0$

Mesh size	Nu_m	Sh_m	Be_m
51*18	5.751221	1.403871	0.54677
102*36	5.875593	1.454238	0.58179
204*72	5.988347	1.499821	0.60548
408*144	6.0073598	1.535326	0.63035
816*288	6.008728	1.534596	0.63005

Table 2. Effects of Reynolds number and Darcy number on the average shear stress ($\frac{\sigma_m.a}{4\mu\bar{k}z}$) Comparison between the current work and those of Alizadeh et al. [5] for $S(\varphi)=\cos(\varphi)$, $Df=0$, $Bi=1000$, $Sr=0$, $Re=5$, $\beta=500$, $\lambda=10$

Re	$\frac{\sigma_m.a}{4\mu\bar{k}z}$		λ	$\frac{\sigma_m.a}{4\mu\bar{k}z}$	
	Alizadeh et al. [5]	Present work		Alizadeh et al.[5]	Present work
0.01	0.09413	0.09286	0	1.43428	1.43057
0.1	0.21868	0.21538	1.0	2.05037	2.05325
1.0	1.43428	1.43286	10	5.64413	5.64112
10	10.65943	10.65435	50	13.52675	13.51987
100	38.12034	38.12351	100	18.75878	18.75131

Table 3. Effects of Prandtl number on the average Nusselt number (Nu_m) for $S(\varphi)=0$, $S(\varphi)=1$ and $S(\varphi)=\cos(\varphi)$, $Df=0$, $Bi=1000$, $Sr=0$, $Re=1$, $\beta=500$, $\lambda=1$

Pr	$S(\varphi)=0$		$S(\varphi)=1$		$S(\varphi)=\cos(\varphi)$	
	Alizadeh et al. [5]	Present work	Alizadeh et al. [5]	Present work	Alizadeh et al. [5]	Present work
0.1	3.59774	3.59183	3.89342	3.89593	3.59124	3.59256
0.4	3.74114	3.72438	5.02176	5.07563	3.76584	3.76081
0.7	3.84888	3.85276	6.20146	6.20651	3.94454	3.94345
1.0	3.93788	3.93021	7.41599	7.41818	4.12699	4.12507
10	5.07670	5.03261	44.32687	44.32112	10.52329	10.52091

Table 4. Effects of Permeability parameter on the average Nusselt number (Nu_m) for $S(\varphi)=0$, $S(\varphi)=1$ and $S(\varphi)=\cos(\varphi)$, $Df=0$, $Bi=1000$, $Sr=0$, $Re=1$, $\beta=500$

λ	$S(\varphi)=0$		$S(\varphi)=1$		$S(\varphi)=\cos(\varphi)$	
	Alizadeh et al. [5]	Present work	Alizadeh et al. [5]	Present work	Alizadeh et al. [5]	Present work
0	3.84219	3.84532	6.19832	6.19352	4.12700	4.12536
1.0	3.84888	3.83106	6.20146	6.20218	4.13656	4.13528
10	3.88851	3.88647	6.22214	6.22101	4.16776	4.16645
50	3.95263	3.95451	6.26340	6.26111	4.19767	4.19436
100	3.98287	3.98546	6.28660	6.28498	4.20916	4.20651

Table 5. Comparison between the current simulations and those of Wang [44] for large porosity and permeability.

η	$Re = 1.0$				$Re = 10$			
	Wang [44]		Present work		Wang [44]		Present work	
	f	$\acute{f}$	f	$\acute{f}$	f	$\acute{f}$	f	$\acute{f}$
1.2	0.02667	0.25302	0.02693	0.25993	0.06638	0.58982	0.06631	0.06610
1.4	0.09665	0.43724	0.09652	0.43710	0.21400	0.84821	0.21393	0.21379
1.6	0.19836	0.57315	0.19828	0.57329	0.39532	0.94852	0.39541	0.39535
1.8	0.32361	0.67444	0.32365	0.67438	0.58919	0.98380	0.58914	0.58926
2.0	0.46674	0.75054	0.46683	0.75046	0.78731	0.99522	0.78735	0.78729

Table6. Comparison between the current simulations and those of Gorla [45] for large porosity and permeability.

Re	f		θ	
	Gorla [45]	Present work	Gorla [45]	Present work
0.01	0.12075	0.12051	0.84549	0.84557
0.1	0.22652	0.22659	0.73715	0.73701
1.0	0.46647	0.46683	0.46070	0.46045
10	0.78731	0.78725	0.02970	0.02983

Table 7. Default values of the simulation parameters

Simulations parameters	η	φ	λ	ε	Re	$S(\varphi)$	Bi	Br	δ	Λ	γ	γ^*	β	Sr	Df	Sc
	1.45	72^0	10	0.9	5.0	$Ln(\varphi)$	0.1	2.0	10	1.0	1.5	1.0	0.1	0.5	1.0	0.1

Table 8. Effects of Reynolds number, Permeability parameter and magnetic parameter on the average shear stress ($\frac{\sigma_m.a}{4\mu\bar{k}z}$) when $Df = 0.1$, $\beta = 0.1$, $Sr = 0.5$, $Re = 10$, $Sc = 0.1$, $\lambda = 10$, $\gamma^* = 2.0$

$\frac{\sigma_m.a}{4\mu\bar{k}z}$							
Re		β		λ		$S(\varphi)$	
0.1	166.8313	0.1	165.9504	1	68.96513	$Ln(\varphi)$	165.9504
1.0	166.7906	1.0	28.37824	10	165.9504	$-Ln(\varphi)$	187.0069
10	165.9504	10	14.54965	100	448.1738	0	176.7695
50	157.3419	100	13.19107	1000	451.8424	1	180.7742
100	145.4965	1000	13.05574	5000	452.3356	-1	172.5796

Table 9. Effects of Biot number and modify conductivity ratio on the average Nusselt, Sherwood and Bejan numbers, $Df = 0.1$, $\beta = 100$, $Sr = 0.5$, $Re = 5.0$, $Sc = 0.1$, $\lambda = 10$, $\gamma^* = 1.5$

Bi	Nu_m	Sh_m	Be_m	γ	Nu_m	Sh_m	Be_m
0.1	3.403892	0.7111769	0.34159	0.1	3.403077	0.7111881	0.41217
1.0	3.297544	0.7123071	0.34204	1.0	3.403613	0.7111807	0.34459
10	3.008347	0.7150651	0.34961	2	3.404159	0.7111733	0.34008
100	2.694756	0.7183075	0.35643	5	3.405554	0.7111548	0.33736
200	2.627727	0.7194447	0.35715	10	3.407310	0.7111322	0.33649

Table 10. Effects of Dufour and Soret numbers on the average Nusselt , Sherwood and Bejan numbers, $Df = 0.1$, $\beta = 100$, $Sr = 0.5$, $Re = 5.0$, $Sc = 0.1$, $\lambda = 10$, $\gamma^* = 2.0$

Df	Nu_m	Sh_m	Be_m	Sr	Nu_m	Sh_m	Be_m
0	3.480933	0.9567361	0.41796	1.0	3.414311	0.9328423	0.44342
0.1	3.411333	0.9569196	0.41537	0.5	3.411333	0.9569196	0.41537
0.4	3.200851	0.9575061	0.40773	0	3.408357	0.9808456	0.38462
0.7	2.987833	0.9581474	0.40018	-0.5	3.405385	1.004621	0.35141
1.0	2.772259	0.9588442	0.39281	-1.0	3.402416	1.028245	0.31652

Table 11 Effects of Reynolds number and Permeability parameter on the average Nusselt, Sherwood and Bejan numbers, $Df = 0.1$, $\beta = 100$, $Sr = 0.5$, $Re = 5.0$, $Sc = 0.1$, $\lambda = 10$, $\gamma^* = 3.0$

Re	Nu_m	Sh_m	Be_m	λ	Nu_m	Sh_m	Be_m
0.1	1.013729	1.329127	0.02603	1.0	3.35902	1.445715	0.81989
1.0	1.385298	1.353001	0.21682	10	3.374974	1.447473	0.52766
10.0	6.008728	1.534596	0.63005	100	3.423083	1.451954	0.10049
50.0	24.54622	1.630741	0.63665	1000	3.477007	1.455629	0.010823
100	41.94905	1.780502	0.65014	5000	3.501193	1.456882	0.002176

Table 12 Effects of Casson fluid parameter and magnetic parameter on the average Nusselt, Sherwood and Bejan numbers, $Df = 0.1$, $\beta = 1.0$, $Sr = 0.5$, $Re = 5.0$, $Sc = 0.1$, $\lambda = 10$, $\gamma^* = 5.0$

β	Nu_m	Sh_m	Be_m	γ^*	Nu_m	Sh_m	Be_m
0.1	1.076977	2.235436	0.18944	0.1	2.215551	0.03038	0.04544
1.0	2.031454	2.329874	0.54705	1.0	2.181737	0.45274	0.16647
10	3.088322	2.413461	0.65497	3.0	2.106596	1.39132	0.40101
100	3.302258	2.428581	0.66761	5	2.031454	2.32991	0.54705
1000	3.32582	2.430213	0.66892	7	1.956313	3.26844	0.63931

Table 13 Effects of Prandtl and Schmidt numbers on average the Nusselt, Sherwood and Bejan numbers, $Df = 0.1$, $\beta = 10$, $Sr = 0.5$, $Re = 5.0$, $Sc = 0.1$, $\lambda = 10$, $\gamma^* = 4.0$

Pr	Nu_m	Sh_m	Be_m	Sc	Nu_m	Sh_m	Be_m
0.1	1.265729	1.904174	0.57602	0.1	3.124834	1.92611	0.59484
0.4	1.843749	1.923239	0.60895	0.3	3.123936	2.103768	0.59351
0.7	2.471502	1.925391	0.61782	0.5	3.121972	2.170684	0.58151
1.0	3.124834	1.926112	0.62484	0.7	3.117515	2.188001	0.54976
10	21.57464	1.929445	0.64321	1.0	3.111808	2.182457	0.50295